TALLINN UNIVERSITY OF TECHNOLOGY
SCHOOL OF ENGINEERING
Department of Materials and Environmental Technology

MICROSTRUCTURE AND MECHANICAL PROPERTIES OF IN-SITU TiB_2 AND TiN_X REINFORCED AlSi10Mg PREPARED BY SELECTIVE LASER MELTING TECHNIQUE

SELEKTIIVSE LASERSULATUSE TEEL IN-SITU VALMISTATUD NING TIB_2 JA TIN_X FAASIDEGA ARMEERITUD ALSI10MG MIKROSTRUKTUUR JA MEHAANILISED OMADUSED

MASTER THESIS

Student: Sanghwa Yi

Student code: KAYM201618

Supervisor: Irina Hussainova, Professor

Co-supervisor: Tatevik Minasyan, Researcher

Tallinn 2022

(*On the reverse side of title page*)

AUTHOR'S DECLARATION

Hereby I declare, that I have written this thesis independently.
No academic degree has been applied for based on this material. All works, major viewpoints and data of the other authors used in this thesis have been referenced.

19.05.2022

Author: Sanghwa Yi
digitally signed

Thesis is in accordance with terms and requirements

20.05.2022

Supervisor: Irina Hussainova
digitally signed

19.05.2022

Co-supervisor: Tatevik Minasyan
digitally signed

Accepted for defence

Chairman of theses defence commission: Sergei Berznnev

Non-exclusive licence for reproduction and publication of a graduation thesis[1]

Sanghwa Yi

1. grant Tallinn University of Technology free licence (non-exclusive licence) for my thesis

MICROSTRUCTURE AND MECHANICAL PROPERTIES OF IN-SITU TiB2 AND TiN_X REINFORCED AlSi10Mg PREPARED BY SELECTIVE LASER MELTING TECHNIQUE

Supervised by Dr. Tatevik Minasyan

1.1 to be reproduced for the purposes of preservation and electronic publication of the graduation thesis, incl. to be entered in the digital collection of the library of Tallinn University of Technology until expiry of the term of copyright;

1.2 to be published via the web of Tallinn University of Technology, incl. to be entered in the digital collection of the library of Tallinn University of Technology until expiry of the term of copyright.

2. I am aware that the author also retains the rights specified in clause 1 of the non-exclusive licence.

I confirm that granting the non-exclusive licence does not infringe other persons' intellectual property rights, the rights arising from the Personal Data Protection Act or rights arising from other legislation.

19.05.2022

[1] *The non-exclusive licence is not valid during the validity of access restriction indicated in the student's application for restriction on access to the graduation thesis that has been signed by the school's dean, except in case of the university's right to reproduce the thesis for preservation purposes only. If a graduation thesis is based on the joint creative activity of two or more persons and the co-author(s) has/have not granted, by the set deadline, the student defending his/her graduation thesis consent to reproduce and publish the graduation thesis in compliance with clauses 1.1 and 1.2 of the non-exclusive licence, the non-exclusive license shall not be valid for the period.*

Department of Materials and Environmental Technology

THESIS TASK

Student: Sanghwa Yi 201618KAYM

Study programme: Materials and Processes for Sustainable Energetics

Main speciality: Process

Supervisor(s): Irina Hussainova

Co-supervisor(s): Tatevik Minasyan

Thesis topic:

(in English) MICROSTRUCTURE AND MECHANICAL PROPERTIES OF IN-SITU TiB_2 AND TiN_X REINFORCED AlSi10Mg PREPARED BY SELECTIVE LASER MELTING TECHNIQUE

(in Estonian) SELEKTIIVSE LASERSULATUSE TEEL IN-SITU VALMISTATUD NING TIB_2 JA TIN_X FAASIDEGA ARMEERITUD ALSI10MG MIKROSTRUKTUUR JA MEHAANILISED OMADUSED

Thesis main objectives:

1. Fabrication of TiB_2 and TiNx reinforced Al matrix composites via selective laser melting of AlSi10Mg/4 and 8 wt.%(Ti+hBN) powders mixture.
2. SLM process parameter optimization.
3. Characterization of the SLM built parts via microstructural analysis, phases composition and investigation of mechanical properties.

Thesis tasks and time schedule:

No	Task description	Deadline
1.	Literature review	15.04.2022
2.	Experiment	29.04.2022
3.	Writing thesis	13.05.2022

Language: English

Deadline for submission of thesis: 23.05.2022

Student: "Sanghwa Yi" 19.05.2022
/digitally signed/

Supervisors: "Irina Hussainova" 20.05.2022
/digitally signed/

Co-supervisors: "Tatevik Minasyan" 19.05.2022
/digitally signed/

Head of study programme: Sergei Bereznev

Terms of thesis closed defence and/or restricted access conditions to be formulated on the reverse side

CONTENTS

PREFACE

This study was conducted at Department of Materials and Environmental Technology at Tallinn University of Technology. The experimental work was carried out at the department of Mechanical and Industrial Engineering. The Master's thesis was prepared under the guidance of Dr. Tatevik Minasyan and Prof. Irina Hussainova. The topic of thesis was proposed by Prof. Irina Hussainova and Dr. Tatevik Minasyan.

I would like to express my sincere gratitude to Dr. Tatevik Minasyan and Prof. Irina Hussainova for teaching, guiding and supporting me.

I would like to thank Dr. Le Liu for introducing me the huge world of additive manufacturing and selective laser melting processes.

I would like to acknowledge my colleagues and all the researchers helping me during my master’s work.

Keywords

Additive manufacturing, Selective laser melting, Aluminum (Al) alloys, in-situ reinforcement, Master thesis

List of abbreviations and symbols

Abbreviation	Full Description
3D	Three dimensional
Al	Aluminum
AM	Additive manufacturing
AMC	Aluminum matrix composite
BJ	Binder jetting
CAD	Computer aided design
CTE	Coefficient of thermal expansion
CSAM	Cold spray lamination manufacturing
DED	Direct energy deposition
DMD	Direct metal deposition
EDS	Energy Dispersive X-Ray Spectroscopy
EBM	Electron beam melting
FDM	Fused deposition modelling
hBN	Hexagonal boron nitride
HV	Vickers hardness number
LPBF	Laser powder-bed fusion
LOM	Laminated object manufacturing
LENS	Laser engineering net shaping
MJ	Material jetting
QC	Quasi-crystal
SLM	Selective laser melting
SEM	Scanning electron microscope
MMC	Metal matrix composite
wt.%	Weight percentage
YAG	Yttrium aluminum garnet
XRD	X-ray diffractometer

Symbol	Explanation
σ_y	Yield strength
σ_u	Ultimate tensile strength
µm	Micrometer
µs	Microsecond
ρ	Density
λ	Wavelength
∅	Diameter
W	Watt
J	Joule
Å	Angstrom

1 INTRODUCTION

1.1 Aluminum (Al) and Al alloys

Demand for lighter, more energy-efficient materials has increased in modern competitive world. Due to low density, high strength/stiffness-to-weight ratio, good corrosion resistance, damage tolerance, ability to be easily processed and heat treated, low cost, as well as excellent electric and thermal conductivity (Table 1), Al alloys have the potential for application and development in the aviation, aerospace, automobile, naval, military and power electronics fields [1]. Al alloys are classified as cast and wrought alloys based on their composition, microstructure and processing characteristics (Fig. 1). Cast Al alloys have 10–12% alloying element content, while wrought Al alloys contain 1–2% alloying element [1]. Al alloys can be further divided into heat treatable and non-heat treatable categories, as shown in Fig.1.

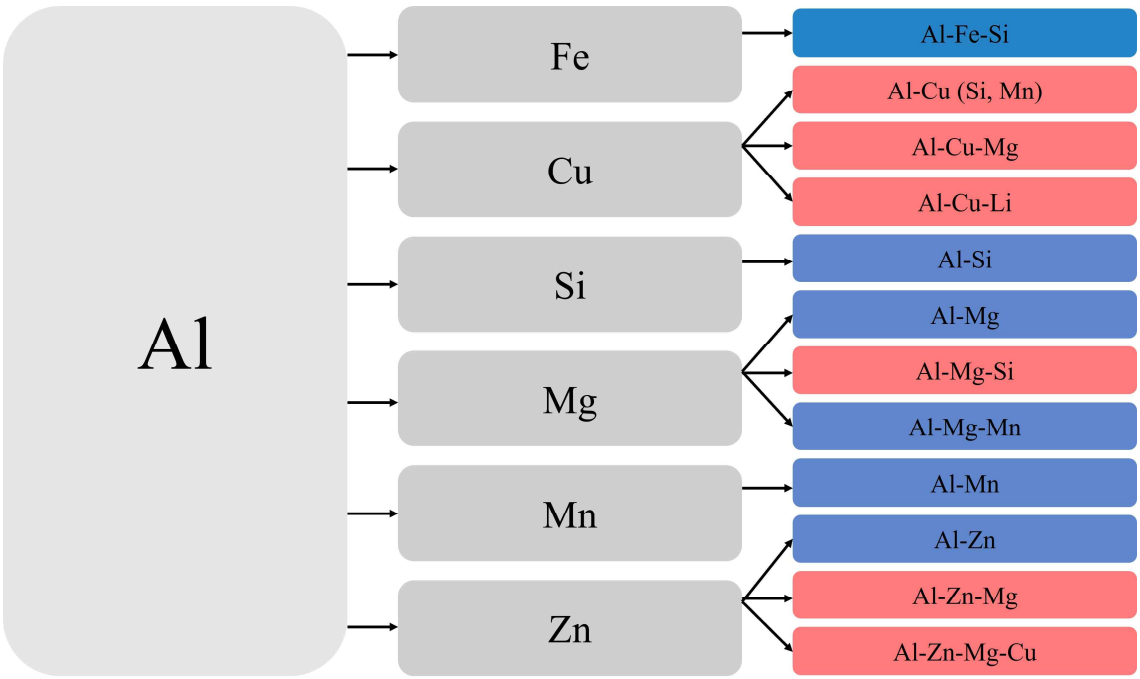

Figure 1. Classification of wrought aluminum alloy. Non-heat treatable Al alloys are in blue and heat treatable alloys are in red [2].

Table 1. Properties of pure aluminum [3]

Properties	Unit	Value
Melting point	K	933
Boiling point	K	2603
Thermal conductivity	W/m/K	94.03
Thermal diffusivity	m^2/s	$3.65x10^{-5}$
Expansion coefficient	1/K	$24x10^{-6}$
Density	kg/m^3	2385
Elastic modulus	N/m^3	$7.1x10^{10}$

Currently, traditional technologies such as casting, forging, extrusion, and powder metallurgy are used to fabricate Al alloy structural parts [4]. However, these processes have obvious limitations, such as (i) coarse microstructure due to low cooling rates, as well as moderate mechanical properties due to offset defects, shrinkage porosity, slag inclusion and element segregation in cast Al alloys, (ii) the preparation and forming processes of high-performance Al alloy components are separated, resulting in a long process chain with limited flexibility and (iii) expensive mould requirement and the complex pre-processes for casting. Furthermore, as modern industrial needs for innovations, the demanding construction and performance requirements of Al alloy parts continue to rise [5][6].

1.2 Additive manufacturing (AM): Selective laser melting (SLM)

Additive manufacturing (AM) technology has the potential to be a game-changer in terms of overcoming the limitations of traditional production techniques. Additive manufacturing, also known as three-dimensional (3D) printing, is a layer-wise fabrication process that allows to manufacture complex shaped objects guided by a digital 3D model, which are otherwise complicated or nearly impossible to produce using conventional manufacturing processes [9].

As a result, AM is a technology that allows designers to fabricate customized or complex models in a single step, reducing material waste and eliminating the need for specialized tooling [7], [8]. Components can also be made on demand, which helps to minimize response time, simplify supply chains, reduce storage requirements, eliminate delivery expenses and shorten lead times for crucial replacement parts [8], meeting a variety of industrial needs (Fig. 2). Owing to the fast response time, it occupies a prominent share in the prototyping processes.

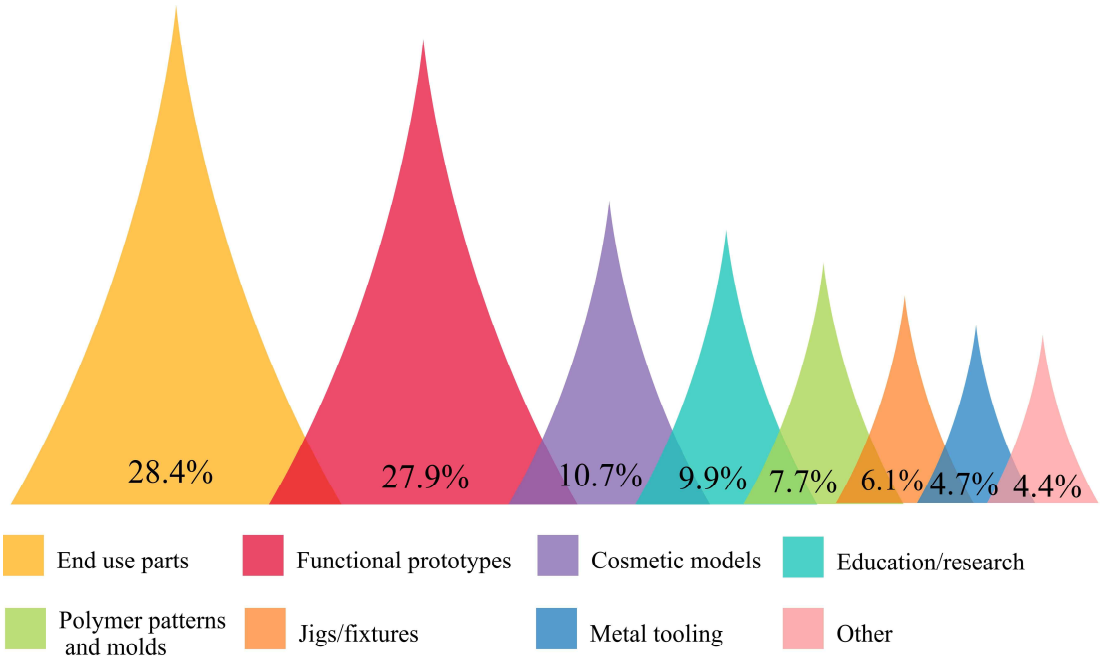

Figure 2. Additive manufacturing state of industry (Wohlers Report, 2019) (adapted from [17])

Several advantages of AM, as shown in Fig. 3, are attributed to the rising consensus of using the 3D manufacturing system over traditional processes, including fabrication of intricate geometry objects with high precision, maximum material savings, design flexibility and personal customization [9].

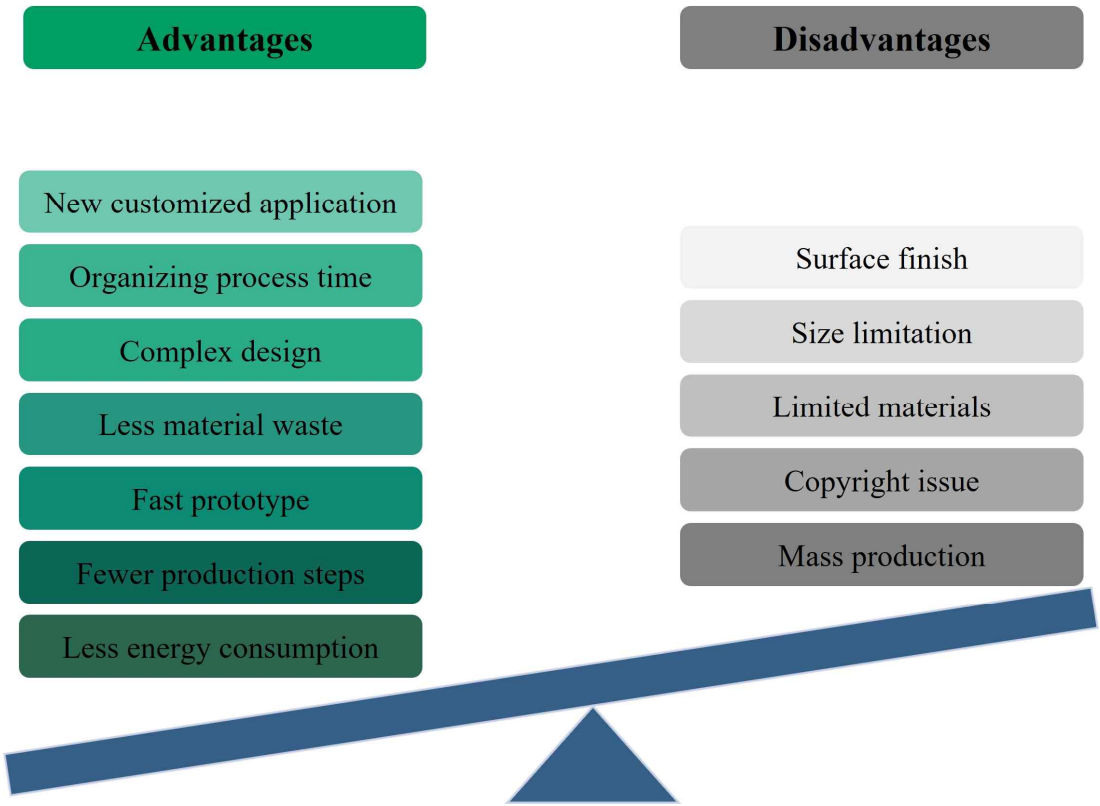

Figure 3. Advantages/disadvantages of additive manufacturing (adapted from [9])

AM technology includes seven different types of processes: vat photopolymerization, material jetting (MJ), binder jetting (BJ), fused deposition modelling (FDM) or material extrusion, powder-bed fusion (PBF), direct energy deposition (DED) and laminated object manufacturing (LOM) (Fig. 4). PBF has 4-subcategories including selective laser melting (SLM), selective laser sintering (SLS), direct metal laser sintering (DMLS) and electron beam melting (EBM).

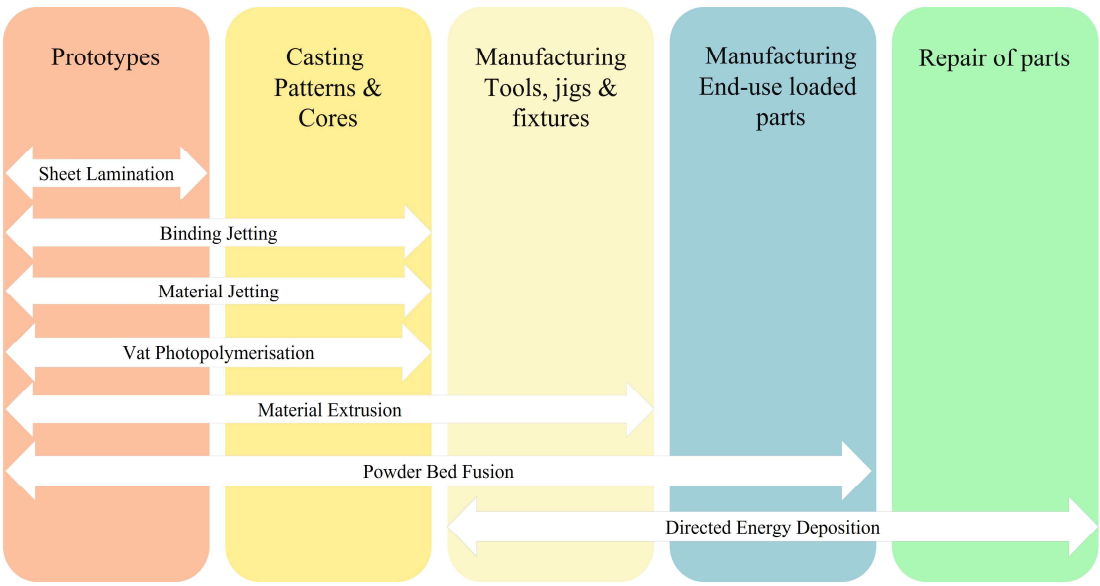

Figure 4. Classification of AM technologies (adapted from [10])

Printing metal products are now the primary concerns by the AM machine manufacturers. Metal printing machines dominate the hardware manufacturers section (47.8%), accounting for 27.3 % of the overall AM machine manufacturing landscape [11]. Automobiles, aerospace applications and, most significantly, research groups use metal printing processes to fabricate novel materials [12]. Biomedical applications, such as human implants, benefit from the printing of personalized metal products [13].

Selective laser melting (SLM)

Selective laser melting or laser powder bed fusion (LPBF) technology is widely used for metal printing for applications such as vehicles, aerospace and biotechnology [14]. Figure 5 depicts the SLM process' premise. The SLM machine inputs the 3D-CAD (computer aided design) volume model, which is split down into individual 2D layers. The target powder is deposited on a substrate (platform) in a defined thin layer. The laser beam then scans the selected sections of the powder based on the geometric information of the individual layers, producing a solid layers of the item to be made. After the scanning process the platform is lowered according the predefined layer thickness value. The manufacturing stages are repeated until the part is completed [15]. Areas that have been scanned by the laser solidify, while areas that have not been scanned will remain powder forms and serve as solid supports. The final product is separated from the unused recyclable powder and cleaned. To prevent oxidation, deterioration, and interaction of the molten material with the environment, the entire production process takes place in aprotective environment such as nitrogen or Argon gas [16].

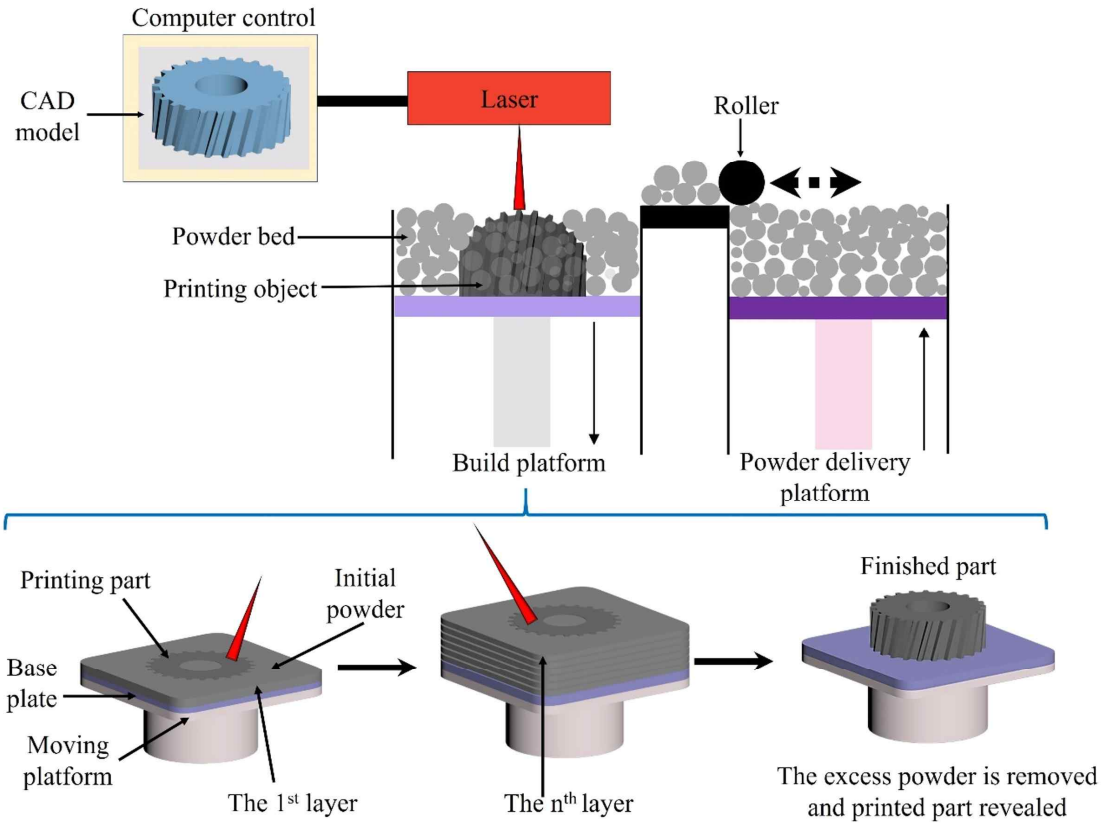

Figure 5. Typical scheme of SLM process (adapted from [17])

The performances of SLMed products are influenced by a number of processing parameters. As demonstrated in Fig. 6, the microstructural characteristics, surface quality and mechanical performance of printed items are all dependent on the precise selection of SLM parameters [18]. Laser type wavelength. effective beam diameter vastly influence the process and the quality of the completed partsthough applied laser powers are same.

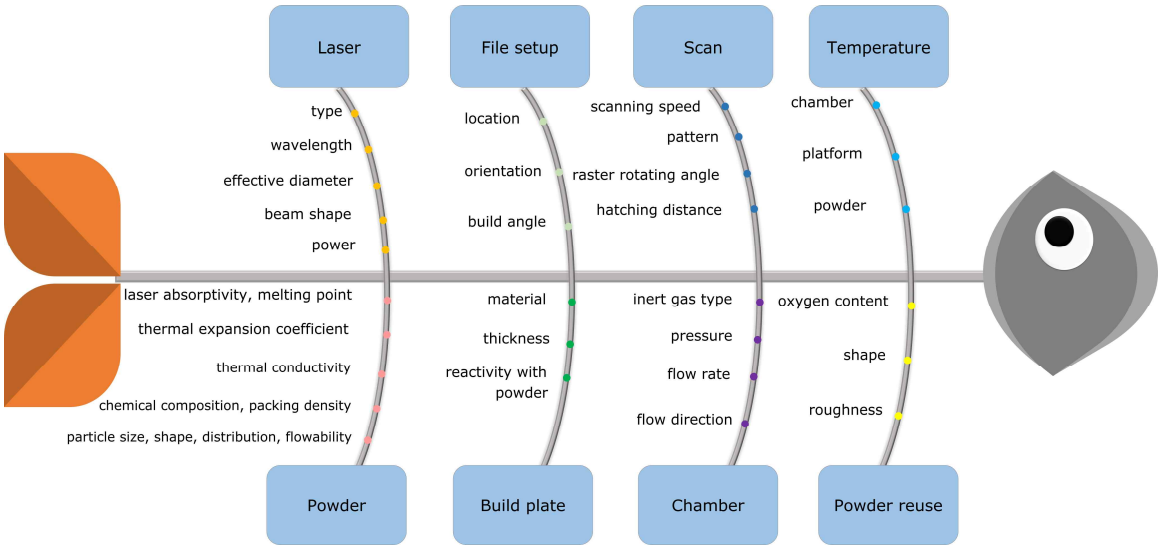

Figure 6. Parameters influencing on SLM outcome (adapted from [18])

The scanning strategy, scanning speed, scanning pattern, angle of raster, hatching distance are crucial variables affecting the SLM process [18]. The material of the build plate, the temperature, powder characteristics, the chamber environment, gas flow are playing dramatic role on the SLM outcome [19], [20]–[22].

Powder requirement for SLM

Size and shape of SLM-applicable powders must be selected carefully due to their impact on powder flowability and deposition, which in their part affect the consolidation process. Below are listed few factors, which are required to consider when choosing appropriate powder feedstocks for SLM process. Powder feedstock appropriate for the SLM process must meet the following requirements [23]:

- Uniform distribution and enhanced powder flowability are provided by homogeneous and dry powders with a spherical morphology. Powders with insufficient flowability and certain level of humidity can cause rough surface finish [24].
- The particle size distribution (PSD) is an essential characteristic that affects operations of SLM fabrication, including powder spreading, storage and recycling [25].
- Preventing oxidation is critical, because oxidation during the laser treatment process induces instability in melt pool and breaks up the melt pool into droplets [26].

- Powder thermal characteristics (thermal absorptivity and conductivity) are detrimental due to the influence of laser absorptivity, melt zone generation and heat transfer mechanisms in the SLM process [27].

Process parameters

In general, the main process parameters in the SLM process are laser power (P), laser scanning speed (ν), hatching distance (h) and layer thickness (t) [28] as seen in Fig. 7.

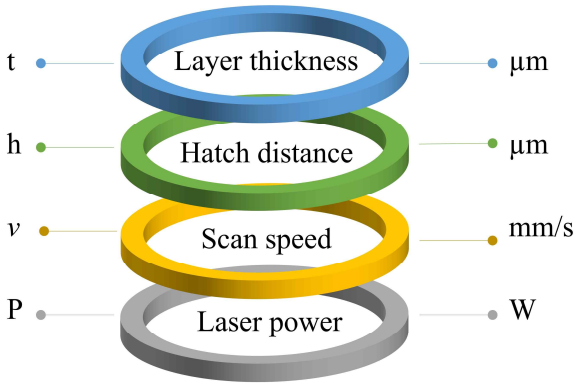

Figure 7. SLM process main parameters: laser power, scanning speed, hatching distance and layer thickness (adapted from [28])

The respective volumetric energy density is calculated according to $E_v = P/vht$ equation. The control and optimization of these parameters result in succesfull process and reliable part properties.

1.3 Reinforcement of Al alloys

There are various near-eutectic Al-Si alloy grades in commercial market that are appropriate for SLM. These materials have good fluidity, thermal conductivity, low coefficient of thermal expansion (CTE) and castability. Hypoeutectic Al-Si (7–12 wt.%)-Mg (>1 wt.%) [29], [30] have the highest percentage of Al alloys suited for SLM processing. Silicon is an essential component in Al-Si alloys because it lowers the melting point and narrows the solidification temperature range by forming a eutectic, which prevents crack formation and propagation. Nonetheless, poor strength, low ductility, moderate fatigue and wear resistance in SLM manufactured Al-Si alloys limit their usage as structural components [31], [32]. Hence, there is an acknowledged need to develop novel aluminum alloys for SLM. The high-strength alloys, previously regarded as "non-weldable materials," suffer from hot cracking along the columnar grain boundaries and posess porosity. Even those that are determined to be "printable"

by SLM technique have a non-uniform microstructure and poor mechanical performance [33]. Anisotropy is a major processing limitation in SLM manufactured parts, driven by the formation of coarse columnar grains with preferential crystallographic orientation along the build direction. Columnar primary Al grains and the eutectic Si phase are the fundamental microstructural features of SLM fabricated hypoeutectic Al-Si alloys. The formation of columnar grains results in intergranular hot tearing and anisotropy in mechanical characteristics. A significant amount of research has been devoted to the following to improve the mechanical performance of SLM produced aluminum alloys:

(i) Developing aluminum matrix composites (AMCs), by adding stable, non-soluble solid ceramic particulates as suitable grain refiners to reduce hot-tear susceptibility, grain growth and dislocation motion [35] [36].

(ii) Investigating the addition of minor alloying components to the existing compositions to develop strengthening phases during manufacturing or post-processing [34].

(iii) Heat treatment [37], [38].

Strengthening methods of adding additives to powders or the surface can be explained by the following mechanisms.

- *Dislocation strengthening mechanism* [39]: High-density dislocations accumulate in the grains and cross tangle as a result of plastic deformation caused by thermal expansion, resulting in increased grain deformation resistance and excellent strength properties, because the thermal expansion coefficient of Al is higher than that of ceramic particles.

- *Orowan strengthening mechanism* [40]: The addition of reinforcement effectively increases the amount of second phase hard inclusions in the specimens, preventing dislocation motion and interface migration. The dislocations pass through second-phase particles during the dislocation slip process, generating dislocation loops and increasing dislocation density, which improves deformation resistance and strength. Furthermore, for particles smaller than 1μm [41], the Orowan strengthening process becomes prominent; the smaller the distance between reinforcements, the more visible the strengthening effect is. In nano-AMC, the mechanism provides considerable advantages.

- *Interface strengthening mechanism* [42]: At the contact interface, mutual dissolution and diffusion between the reinforcement and the molten Al generate a new phase, converting the bonding type property from mechanical to chemical. The interface bonding improves the AMCs' strength.

- *Fine crystal strengthening mechanism* [43]: The addition of reinforced particles and a high cooling rate are advantageous in the SLM process for obtaining a fine microstructure of AMCs. The reinforced particles at the liquid–solid boundary lower interfacial energy, constrain the liquid–solid boundary's fluidity and stabilize the grain boundary, preventing grain growth. The reinforced particles at the solid–liquid interface, as well as the in-situ formed phase during chemical reactions are exploited as nucleation sites, promoting heterogeneous nucleation and grain refinement.

Reinforcement of Al alloys by ceramic additives

Due to their high melting temperatures and chemical stability, non-oxide ceramics (borides, carbides, nitrides, etc.) are one of the most frequently applied reinforcements for Al alloys [44]. AMCs combine aluminum's ductility with the high hardness and strength of the ceramic reinforcements, resulting in improved overall properties. Al alloys are widely recognized for having low laser absorptivity in the infrared spectrum, which makes controlled melting difficult. The laser absorptivity of the Al alloy can be increased by adding non-oxide ceramic particles. Figure 8 indicates that adding TiC and TiB_2 to AlSi10Mg alloy increases laser absorptivity by almost 1.5 times [45].

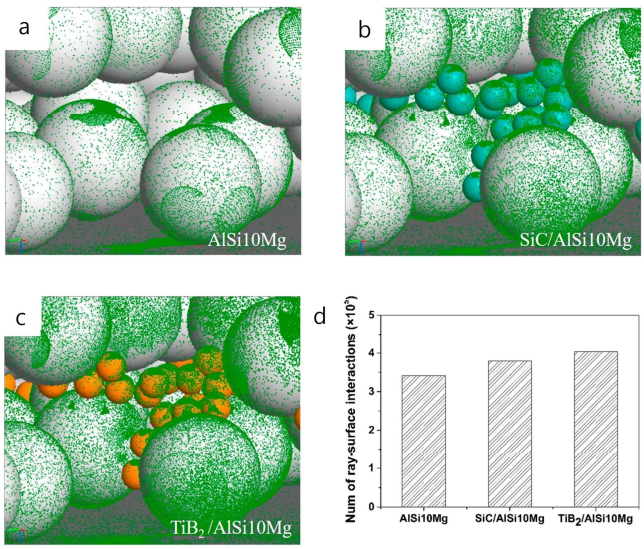

Figure 8. Track spot of lasers ray on the particles surface of AlSi10Mg (a), SiC/AlSi10Mg (b), TiB_2/AlSi10Mg (c) and the number of ray-surface interactions (d) [46]

Both ex-situ and in-situ ceramic reinforcing methods are both well acknowledged for fabrication of AMCs. However, the formation of chemically stable reinforcing compounds, contaminant-free reinforcement/matrix interfaces and additional thermal energy for fusion provide advantages of in-situ reinforcement over ex-situ one. Meanwhile, the in-situ formed compounds may dissolve in a metal matrix, causing significant embrittlement; the generated extra heat of the chemical reaction could induce melt pool instability, resulting in powder splash and gas evaporation. As a result, investigations should be conducted prior to the SLM process to estimate the benefits and disadvantages of both in-situ and ex-situ reinforcing options.

Generally the addition of stable grain refiners with the lowest allowable lattice mismatch with aluminum is employed for grain refining of Al alloys. The grain refiners reduce columnar grain formation, promote the generation of fine, equiaxed grains [47]. During solidification, heterogeneous nucleation of α-Al occurs primarily on the grain refiners, which serve as low-energy interfaces between a refiner and a matrix. The number of effective grain refiners among thermally stable compounds is limited, and those with the minimum lattice mismatch are preferred [48]. Both in-situ generated and added refiners have the ability to promote heterogeneous nucleation of Al grains when the lattice mismatch value is less than 10% [49]. The influence of several ceramics on the properties and microstructure of AMCs is described below.

As described in [23], in comparison with the SLMed unreinforced AlSi10Mg counterparts, the 3.4wt.% TiB_2/AlSi10Mg composite showed refined microstructure and no crystallographic texture (Fig. 9d and e). On the grain boundary, the in-situ formed TiB_2 particles were evenly dispersed. The acicular eutectic Si phase developed into fine spherical particles, forming the grain boundary networks and nano Si precipitates in the cells. The SLMed TiB_2/AlSi10Mg composite has a tensile strength of 451 MPa, and an extraordinary microhardness of 151 HV0.1, outperforming the as-cast TiB_2/AlSi10Mg composite and the SLMed AlSi10Mg alloy (Table 2).

In [51], the in-situ $D0_{22}$-Al_3Ti phase was formed in TiC/AlSi10Mg composite during SLM process (Fig. 9a). $D0_{22}$-Al_3Ti was known to be more effective nucleant than TiC to promote the heterogeneous nucleation of α-Al. The SLMed TiC/AlSi10Mg alloy, in contrast to the SLMed AlSi10Mg alloys, has fine equiaxed grains and textureless microstructure (Fig.9f and g). The latter occurs, because both TiC and D_{022}-Al_3Ti nanoparticles had a low atomic mismatch with the Al matrix, lowering the critical undercooling for heterogeneous nucleation and promoting Al nucleation on TiC and $D0_{22}$-Al_3Ti nanoparticles. The AlSi10Mg alloy reinforced with 5wt.% TiC nanoparticles has higher tensile strength and yield strength (σ_u=456 MPa, σ_y= 338 MPa) and microhardness (131 HV) than the unreinforced alloy (Table 2).

In AlSi10Mg/2wt.% nano-TiN system [52], mutual diffusion and in-situ interaction between TiN clusters and matrix were observed. Under the driving force of the liquid flow, the unmelted TiN particles reorganized before being equally dispersed in the Al matrix (Fig. 9b). The in-situ TiN-Al reaction created a graded interfacial layer with a certain thickness between reinforcing TiN cluster and Al matrix. The micro-hardness of TiN containing composite was measured as 145±4.9 HV0.1 added composite, which is higher, than hardness of AlSi10Mg alloy (125 ± 4.8 HV0.1). The AMCs' hardness and wear resistance were considerably improved by the combined impacts of reduced grain size and in-situ formed graded layer.

Mechanical properties of AMCs reinforced with SiC and Si_3N_4 ceramic particulates were also notably improved. Nanohardness, tensile strength and elongation of AlSi7Mg/nano-SiC composite was remarkably enhanced. The strength was increased due to the solid solution strengthening, grain refinement (Fig. 9 h, i) and the presence of nanosized Si, Mg_2Si and in-situ formed Al_4C_3 phase (Fig. 9c) at the cell borders.

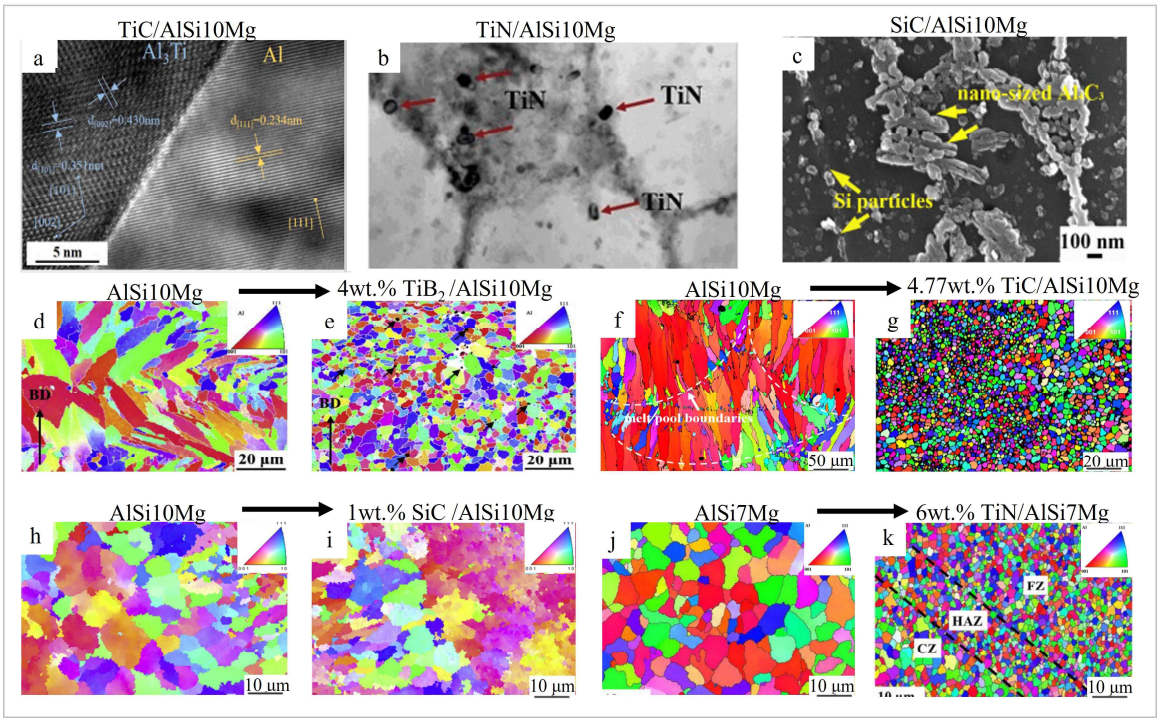

Figure 9. The HRTEM image of $D0_{22}$-Al_3Ti/Al matrix in TiC/AlSi10mg composite (a)[51], SEM image of TiN nanoparticles in Al matrix in TiN/AlSi10Mg composite (b)[52], SEM image of in-situ formed Al_4C_3 nanoparticles in SiC/AlSi10Mg composite, (c). EBSD color maps of AlSi10Mg and AlSi10Mg/4wt.%TiB_2 (d and e); AlSi10Mg and AlSi10Mg/4.77wt.%TiC (f and g), AlSi10Mg and AlSi10Mg/1wt.%SiC (h and i); AlSi7Mg and AlSi7Mg/6wt.%TiN (j and k) [53]–[56].

Table 2. Mechanical properties of Al alloys with ceramic reinforcements by SLM.

System	Used device, Process parameters	Relative density (%)	Average grain size (μm)	Strength (MPa)	Elongation (%)	Vicker's hardness (HV)	Ref.
AlSi10Mg	SLM125HL P=300 W v=1650 mm/s t=30 μm h=130 μm	99.08 ±0.10	6.1	σ_u=370 σ_y=200	7.0 ± 0.8	-	[57]
AlSi10Mg+ 2wt.% LaB_6		99.48 ±0.22	0.8	σ_u=429 σ_y=243	3.7 ± 1.1		
AlSi10Mg	EOS M280 P=270 W v=1600 mm/s t=30 μm h=110 μm	99.22	12.1	σ_u= 393.8 ± 14.5 σ_y =242.2 ± 7.2	4.5 ± 0.9	127 ± 2.4 HV0.1	[58]
AlSi10Mg+ 1.5 wt.% TiB_2+ 1.5 wt.% TiC		99.02	1.5	σ_u= 552.4 ± 12 σ_y =325 ± 10	12 ± 0.6	142 ± 2.9 HV0.1	
AlSi10Mg+ 3 wt.% TiB_2		97.12	7.7	σ_u= 360.6 ± 8.5 σ_y =325 ± 10	3.8 ± 0.2	134.4 ± 1.4 HV0.1	
AlSi10Mg+ 3 wt.% TiC		98.23	1.7	σ_u= 453 ± 10 σ_y=267.5 ± 7.8	4.8 ± 1.1	138.3 ± 1.7 HV0.1	
AlSi7Mg	EOSINT M280 P=350W v=1200mm/s t=40 μm h=190 μm	99.41	1.30	σ_u= 388.31	7.03±1.25	Nano hardness 1.85±0.06 GPa	[59]
AlSi7Mg + 2 wt.% nano-SiC		99.75	1.28	σ_u= 502.94	10.64±1.6	Nano hardness 2.21±0.2 GPa	
AlSi10Mg	SLM apparatus P=200 W v=100-300 mm/s t=30 μm h=60-100 μm	99	-	-	-	-	[60]
AlSi10Mg+ 1wt.%AlN		97	2				

AlSi10Mg	EOSINT M290 P=380 W v=1300 mm/s t=30 µm h=200 µm	99.85	-	σ_u=165	-	103 HV0.2	[61]
AlSi10Mg+ 1wt.%BN		99.19		σ_u=230		136 HV0.2	
Al2024	EOS M290 P=200 W v=100 mm/s t=40 µm h=90 µm	98.2	1.0~87	σ_u=240± 10	0.3±0.2	108 HV0.2	[62]
Al2024 + 1 wt.% TiC + 1wt.% TiH_2		97.1	0.3-6.3	σ_u=390± 15	12.0±0.5	120 HV0.2	

P-laser power, v-scanning speed, h-hatching distance, t-layer thickness, σ_u *- ultimate tensile strength,* σ_y *-yield strength*

Even though the added ceramic particulates promote grain refinement and improvement in mechanical properties, however they mights reduce the densification level, as observed in case of dual TiC-TiH_2, AlN and BN addition (Table 2). Hence the amount of ceramic phase, size and distribution should be carefully considered prior to SLM process.

Modification of the Al alloy composition

The microstructure and mechanical properties of Al alloys are influenced by the lattice structure and size of each alloying element. Major and minor elements, microstructure modifiers and impurities are all types of alloying elements; however, impurity elements in certain alloys may be major elements in others. The effects of major alloying elements (Si, Cu, Mg), minor alloying elements (Ni, Zn), microstructure modifier elements (Ti, B, Sr, Be, Mn, Cr) and impurity elements (Fe, Zn) on the microstructures and mechanical characteristics of aluminum alloys are briefly discussed below [63]. As seen in Fig. 10, each element plays unique role in the process and for properties of the Al alloy.

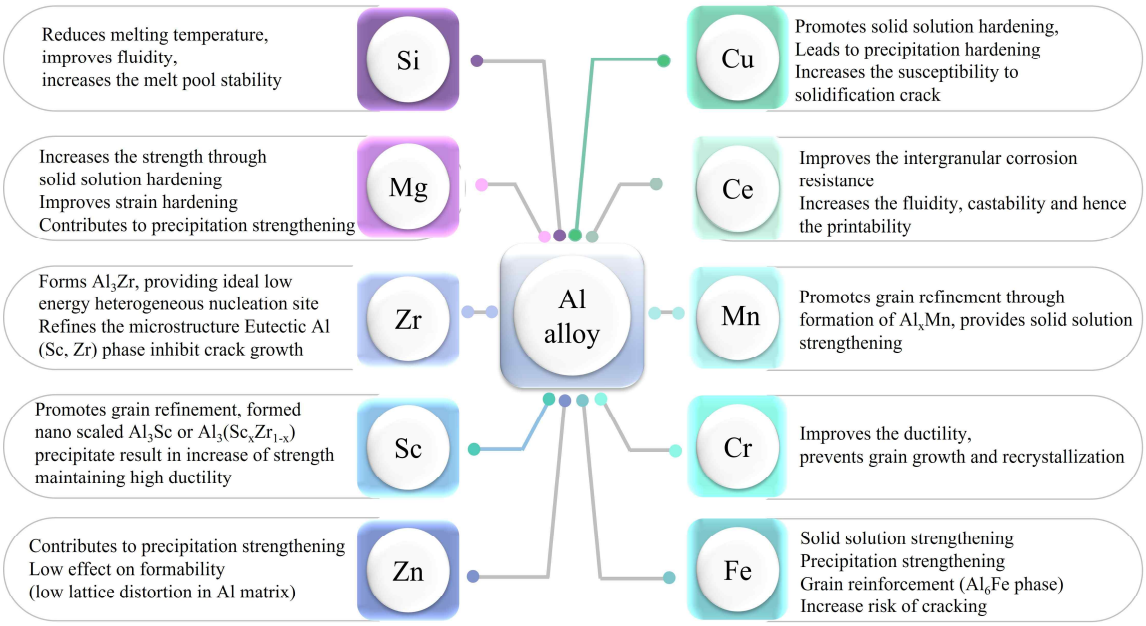

Figure 10. Role of each alloying element in process and properties of Al alloys (Si [37],Mg [38], Zr [39], [40], Sc [40], Zn [41], Cu [42], Ce [43], Mn [44], [46], Fe [45], Cr [47]) (adapted from [75])

In [73] it was shown, that the addition of 5wt.%Fe to Al-12Si significantly improved the hardness), however, due to the limited compatibility and miscibility, the Fe/Al-12Si composite bulks experience cracking.

It was studied that the addition of Fe to Al-11.6Si-0.97Cu-0.96Mg-1.0Ni-0.1Fe alloy resulted in improved high-temperature strength while keeping good ductility [72]. Because of high cooling rate, Fe was disseminated as fine Fe-Si-Ni particles, promoting grain refinements.

When added Fe to Cr containing Al alloy (Al25Cu-10Fe-5Cr), as shown in [76], Fe-Cr quasi-crystal (QC) structures were developed in Al matrix, which serve as nucleation centers.

Sc and Zr can be used as additives to avoid cracking. In [77] were investigated the multiple effects of Sc/Zr elements in selective laser melted Al alloy. The Sc/Zr elements addition resulted in in-situ formation of Al_3Sc, Al_3Zr, or $Al_3(Sc,Zr)$ phases which prevent solidification, promote the grain refinement, reduce the textureing and results in isotropic mechanical properties (Table 3).

In [55], it was shown that adding Zr to Al-4.24Cu-1.97Mg-0.56Mn alloy results in formation of Al_3Zr and in significant grain refinement, however to a certain 2wt.% content of Zr. The further addition of Zr does not result in further grain refinement (Fig. 11 e-h). Meanwhile nano ZrO partcles can be formed, which can also serve as

grain refiners. By adding 2 wt. Zr to Al alloy, the σ_u= 493.3 MPa and σ_y=464.06 MPa were achieved, however the increase in Zr content resulted in decrease in strenghth.

In [78] SLM was successful in producing dense and crack-free Al 7075 parts by adding Si. The addition of Si can reduce the melting temperature, enhancing the alloy's fluidity. The addition of 4wt.%Si, prevents the formation and propagation of cracks, and leads to substantial grain refinement as illustrated in Fig.11a-d.

Hence, it can be observed, that in-situ composition modification of metallic powders for SLM processing is favorable [79].

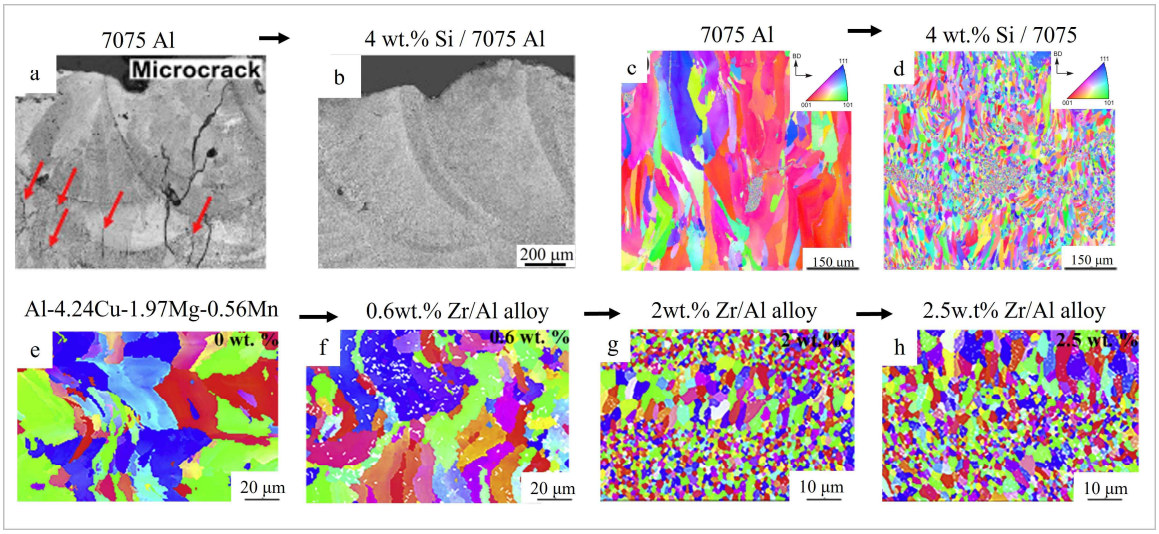

Figure 11. SEM images of 7075 Al (a) and 4wt.%Si/7075 Al (b) [80], EBSD color maps of 7075 Al alloy (c) and 4wt.%Si/7075 Al (d). EBSD color images of Zr modifed Al-Cu-Mg-Mn alloy (e-h) [81]

As shown in Table 3, the element additives remarkably influence the mechanical properties of Al alloys. The [69] and [85] studies represent that the mechanical properties of aluminum alloys change according to Cu and Ni additive content, respectively. For 4.5 wt.%Cu/Al alloy, which has very high ductility, the true strain decreased from 33% to 2.5%, as the Cu content increased to 33 wt.%.

Table 3. Mechanical properties of Al alloys modified with element additives

System	Used device, Process parameters	Relative density (%)	Average grain size (um)	Strength (MPa)	Elongation (%)	Vicker's hardness (HV)	N
7xxx (Al-Zn-Mg-Cu) alloy 9.10wt.%Zn 2.33w.t%Mg 1.48wt.%Cu	Solutions 250HL P=190W laser v=155 mm/s t=70μm h=50μm	99.8	~50	σ_y =132	-	123 HV0.1	[83]
7xxx/**Si-**Fe-Ni 12 wt.%Si, 1.4wt.%Fe, 1.4wt.%Ni			~2	σ_y =219		186 HV0.1	
Al-Mg-Cu alloy	FS271 M P=300W v=800mm/s t=50μm h=120μm	-	20~30	σ_y =93	-	130 HV0.1	[84]
Al-Mg-Cu alloy/**Si-Zr** 7wt.%Zn, 3wt.%Mg, 1wt.%Cu, 2.9wt.%Cu, 1wt.%Zr		97.3	2.93	σ_y =350	6.7	161 HV0.1	
Al-3.1**Ni**	FS271 P=350W v=1500 mm/s t=30μm h=100μm	99.85	2~10	σ_u =308 σ_y =120	14	-	[85]
Al-5.7**Ni**			1~5	σ_u =407 σ_y =278	9.5		
Al-4.5**Cu**	SLM 250HL P=190 W v=165 mm/s t=40 μm h=80 μm	> 99	-	σ_u <400	ε_t =33	-	[69]
Al-20**Cu**				σ_u =870	ε_t =7.5		
Al-33**Cu**				σ_u ~1000	ε_t =2.5		

P-laser power, v-scanning speed, h-hatching distance, t-layer thickness, σ_u *- ultimate tensile strength,* σ_y *-yield strength,* ε_t *-true strain*

Reinforcement of Al alloys by heat treatment

The distinctive solidification circumstances experienced by molten metal during the SLM process, as well as the layer-wise feature of the process, result in a range of microstructural peculiarities, such as the development of metastable phases and supersaturated solid solutions, microstructural refinement and the generation of residual stresses. As a result, post-build heat treatments, which are routinely used on conventionally produced aluminum alloys, may need to be tweaked to accommodate the unique metallurgy of SLMed Al alloys and address the issues related to the process[86].

The purpose of the heat method is to modify microstructures in order to change mechanical properties to meet the industrial requirements. As a result, while designing a heat treatment method, both the initial and final microstructures should be considered [87]. Heat treatment of Al alloys can be used to eliminate residual stresses (stress relieving), to optimize the mechanical properties such as ductility, machinability and structural stability (by annealing), or to improve a specific mechanical attribute, such as tensile strength or fatigue strength (by solution treatment and ageing) [88].

As shown in [38], the annealing of AlSi10Mg alloy samples at 300°C for 2h was effective to remove the residual stresses and enhance the overall mechanical properties of AlSi10Mg alloy and increase the elongation up to 15.3 %. The change in microstructure, or the diffusion of the well-dispersed Si to produce coarser particles, caused variation in nano-hardness across the material after heat treatment. The microstructure is no longer ultrafine-grained after heat treatment, as seen in Fig. 12a and b, which reduces the contribution of grain boundaries to strengthening.

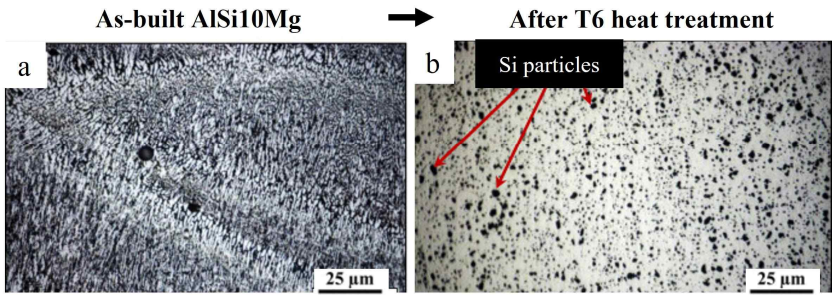

Figure 12. Opitcal microscope images of the SLM prepared AlSi10Mg before (a) and after heat treatment (T6) (b) [38].

In [89], [90] after traditional (T6) heat treatment of the SLMed AlSi10Mg, the fracture features have been coarsened as seen in the dimpled surface in Figure 13b, while the as-built sample fracture shows equixed finer dimples indicating micro-void coalescence and deformation by slip.

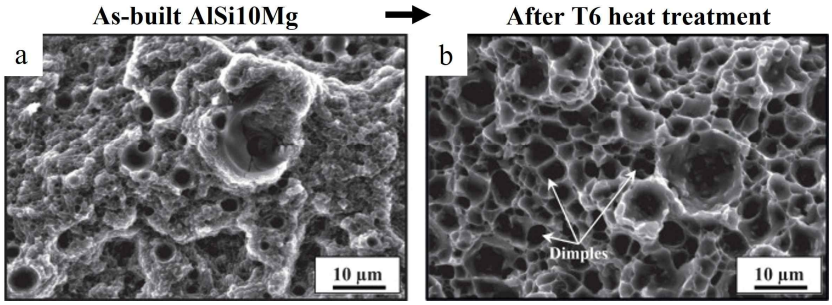

Figure 13. SEM images for the fracture surface of SLM prepared AlSi10Mg: as-built (a) and heat treated(b) [38].

1.4 Objectives

In this research, the effects of in-situ formed TiB_2 and TiN_x on the microstructure and mechanical properties of AlSi10Mg were investigated. The main objectives of this work are:

1) Fabrication of TiB_2 and TiNx reinforced Al matrix composites via selective laser melting of AlSi10Mg/4 and 8 wt.%(Ti+hBN) powders mixture.

2) SLM process parameter optimization.

3) Characterization of the SLM built parts via microstructural analysis, phases composition and investigation of mechanical properties.

2 Materials and methods

In this work, two powders mixtures of AlSi10Mg/4wt.%(Ti+hBN) and AlSi10Mg/8wt.%(Ti+hBN) were prepared by mixing AlSi10Mg (Fehrmann alloys, 20-63 μm), Ti (Alfa Aesar, <20μm, >99%) and hBN (Aldrich, <10 μm, >99.5%) precursors. At first Ti and hBN powders were mixed for 5 hours, afterwards the AlSi10Mg/(Ti+hBN) mixtures were prepared by mechanical rotation mixing for 24 hours in atmospheric conditions.

Table 4 shows the powder composition of commercially available AlSi10Mg. Table 5 shows the content of additives in the AlSi10Mg/4wt.%(Ti+BN) and AlSi10Mg/8wt.%(Ti+BN) powders mixtures. The Ti:BN ratio was chosen according to the $3Ti+2BN = TiB_2+2TiN$ reaction, considering the reagents react completely.

Table 4. Elemental composition of the commercial AlSi10Mg powder (Fehrmann Alloys GmbH & Co)

Al	Si	Fe	Cu	Mn	Mg	Ni	Zn	Pb	Sn	Ti
Balance	9.0-11.0	<0.55	<0.05	<0.45	0.25-0.45	<0.05	<0.10	<0.05	<0.05	<0.15

Table 5. Composition of each powder mixture

System	Weight percent of the reagents (wt. %)		
	AlSi10Mg	Ti	BN
AlSi10Mg+4wt.%(Ti+BN)	96	2.97	1.03
AlSi10Mg+8wt.%(Ti+BN)	92	5.94	2.06

Thermodynamic calculations were performed by Thermo-calc, Isman Thermo and HSC 5 software to study the possible reaction in AlSi10Mg-Ti-BN system.
SLM280 (SLM Solutions, Germany, table 6) equipped with ytterbium laser was utilized for feedstock powders consolidation.
Cylindrical samples with ∅7 mm × 7 mm dimensions were designed for the SLM experiments. Samples were numbered according to the SLM processes parameters shown in Table 7, applying fixed 350 W laser power (P). Scanning speeds (v) were set 700, 850, 1000, 1150, 1300 $mm \cdot s^{-1}$. Layer thickness (t) was chosen as 30 μm and hatching distance (h) as 170 and 100 μm. The laser volumetric energy (E_v) was calculated according to $E_v = P/t \cdot h \cdot v$ To prevent oxidation, high purity (≥99.99 %) argon gas flow was employed throughout the operation.

Table 6. Technical specifications of SLM-280 apparatus

Equipment	SLM-280
Build envelope dimension (L x W x H)	280 x 280 x 365 mm
Variable layer thickness	20 - 90 µm
Laser power	400W – 1kW
Beam focus diameter	80 - 115 µm
Average inert gas consumption	13 l/min(Argon)
Laser type	Dual 700W fiber laser
Wavelength	1064nm

AlSi10Mg sample was prepared as a reference and labelled as So. For So optimized parameters suggested from SLM Solutions were used.

Table 7. SLM process parameters for consolidation of AlSi10Mg+4wt.%(Ti+BN) and AlSi10Mg+8wt.%(Ti+BN) powders mixtures

System		Process parameters				
AlSi10Mg/ 4wt.% (Ti+hBN)	AlSi10Mg/ 8wt.%(Ti+hBN)					
Sample labels		Laser power (W)	Scanning speed (mm/s)	Hatching distance (µm)	Layer thickness (µm)	Volumetric energy density (J/mm^3)
S_4-1	S_8-1	350	1300	170	30	52.8
S_4-2	S_8-2	350	1150	170	30	59.7
S_4-3	S_8-3	350	1000	170	30	68.6
S_4-4	S_8-4	350	850	170	30	80.7
S_4-5	S_8-5	350	700	170	30	98.0
S_4-6	S_8-6	350	1300	100	30	89.7
S_4-7	S_8-7	350	1150	100	30	101.4
S_4-8	S_8-8	350	1000	100	30	116.7
S_4-9	S_8-9	350	850	100	30	137.3
S_4-10	S_8-10	350	700	100	30	166.7

The density of the SLM prepared samples was measured using the Archimedes method (Mettler Toledo ME204 density kit, Australia). The samples were polished following standard mettalographic procedures using auto-polishing system (Buehler/ MetaServ 250 & Vector, USA). The microstructural analyses were performed using Pixelink PL-A662 optical microscope (OM) and Zeiss EVO MA15 scanning electron microscope (SEM) equipped with INCA Energy EDS detector. Phase identification of the samples was conducted by X-ray diffractometer (Siemens/Bruker, D5005 (USA) with CuKα1 radiation (λ= 1.5406 Å).

The samples were etched for 20-30 seconds using Keller reagent (solution of 1 ml HF, 1.5 ml HCl, 2.5 ml HNO_3 and 95 ml of distilled water). For the hardness measurement, 1 kgf load was applied for 10 seconds using Indentec 5030 SKV apparatus. For each sample, five indentations were performed, and the average value was selected along with the standard deviation.

3 Results

Thermodynamic calculations were performed to study the possible reactions in AlSi10Mg-Ti-BN system. The change in Gibbs free energy (ΔG, equation is shown below) reactions are computed using HSC software and existing thermodynamic data (Fig. 14).

$$\Delta G = \Delta H - T\Delta S$$

Where ΔH is the change of enthalpy, ΔS is the change of entropy and T is the temperature.

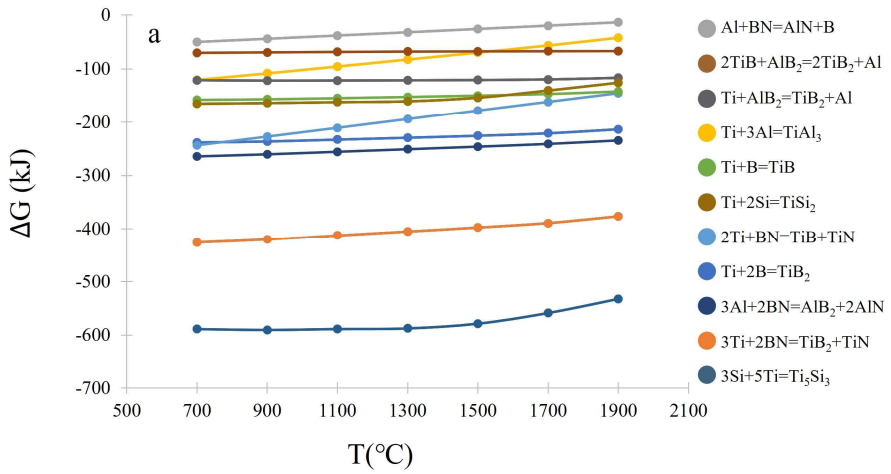

Figure 14. The variations of Gibbs free energy (ΔG) versus temperature for plausible chemical reactions

In the range of 700–1900°C the Gibbs free energy is negative for all above written chemical reactions, as seen in Fig. 14. However, it is significantly lower for the $3Ti+2BN=TiB_2+2TiN$ and $3Si+5Ti=Ti_5Si_3$ reactions, meaning that those are thermodynamically favorable to take place.

Fig. 15a and b show the binary Al-Si phase diagram and isothermal section of ternary Al-Si-Ti system at 600°C.

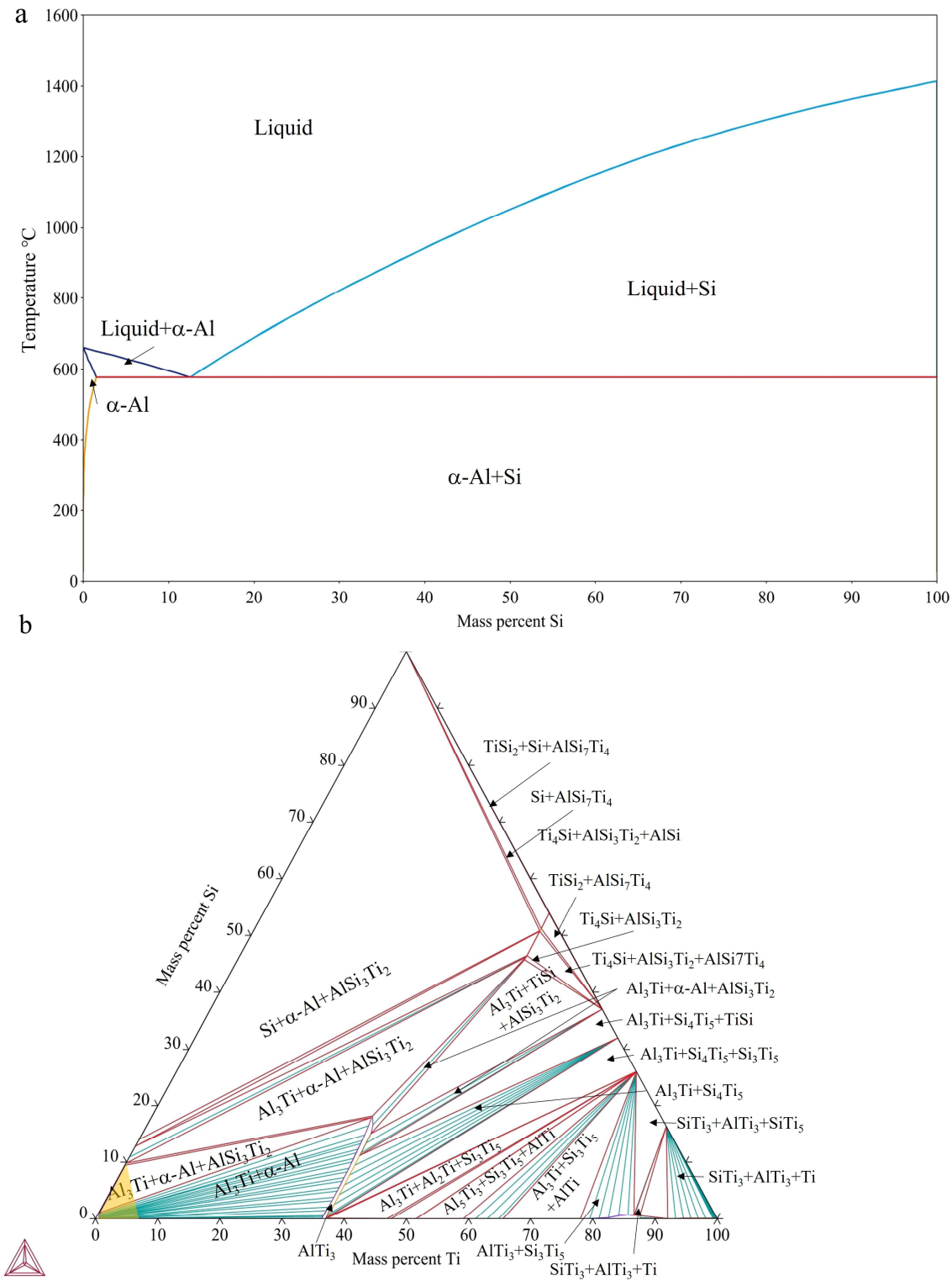

Figure 15. Al-Si binary phase diagram (a) and isothermal section of ternary Al-Si-Ti system at 600℃ (b).

According to isothermal section of Al-Si-Ti ternary system (Fig. 15b) Al_3Ti and $AlSi_3Ti_2$ phases are formed at high Al contents (the area highlighted with orange triangle represents the target composition chosen in this work).

The thermodynamic calculations were performed for the 3Ti+xBN mixture to estimate the adiabatic temperature, the possibility of in-situ interaction of additives under laser agitation and the content of formed products. dependent on the content of the BN (x) on relation to Ti (3 moles) different reagents are formed altering the calculated adiabatic temperature of the reaction. Increasing the BN content up to 1.2 mole, the unreacted Ti is decreasing and already at 1.6 mole of BN, the system contains TiN, TiB_2 and TiB (Fig. 16a). Increasing the BN content to 2 moles, all TiB is transformed to TiB_2 and the adiabatic temperature reaches to 2350℃. Sufficient exothermicity of the target reaction indicates the feasibility of in-situ or reactive laser sintering. Further increase in BN content decreases the reaction temperature as the excess BN serves as thermal diluent (Fig. 16b).

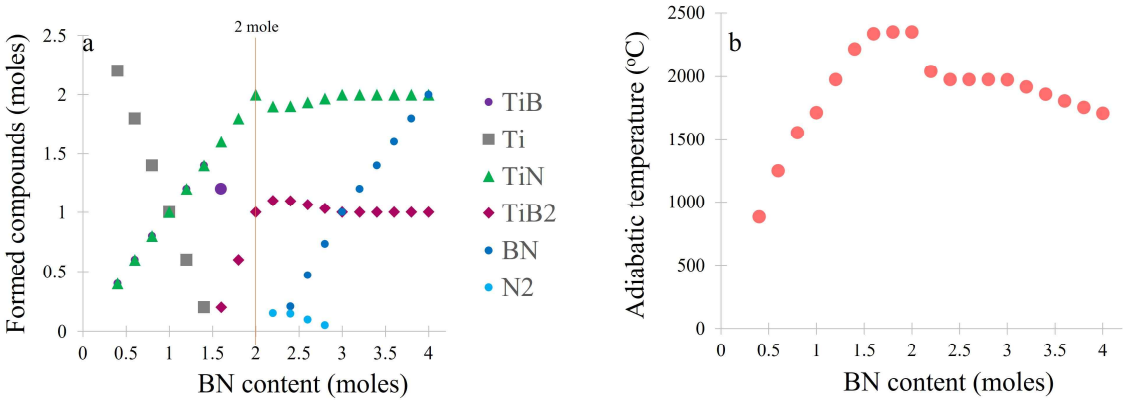

Figure 16. Thermodynamic modeling of Ti+BN system. The influence of BN content on the equilibrium composition of products (a) and the adiabatic temperature (b).

Based on thermodynamic considerations, the bulks were SLM fabricated.

SEM images exhibiting the morphologies of pure AlSi10Mg, hBN and Ti powders are presented in Fig. 17a-g. The powder feedstock is composed of spherical Al alloy powders, hBN flakes and irregular shaped Ti powders. The SEM image of S_4 powder mixture is shown in Fig. 17h-m.

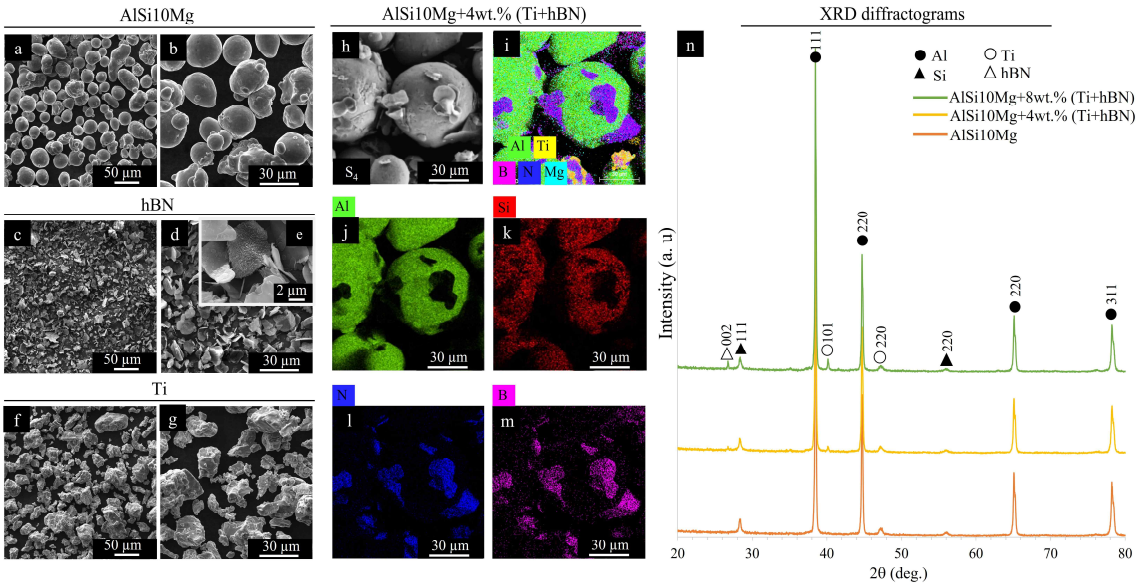

Figure 17. SEM images of AlSi10Mg (a, b), hBN (c-e), Ti (f, g) powders, S_4 powder mixture (h) with respective mixed map (i-m) and XRD diffractogram of feedstock powders (n).

The EDS elemental and mixed maps of S_4 mixture illustrates hBN microflakes are decorating the AlSi10Mg and Ti powder (Fig. 17n). XRD patterns of the AlSi10Mg/4-8wt.% (Ti+hBN) blended mixtures show the respective peaks of the Al, Si, Ti and hBN (Fig. 17n).

When analyzing the bulk samples prepared by SLM, it was observed that the densities of printed samples are affected by the applied volumetric energy density values, as shown in Fig. 18 a, b. And regardless of the content of the ceramic additives, the tendency of density variations is similar. A significantly low-density values are measured when $E_V \geq 98$ J/mm^3.

.

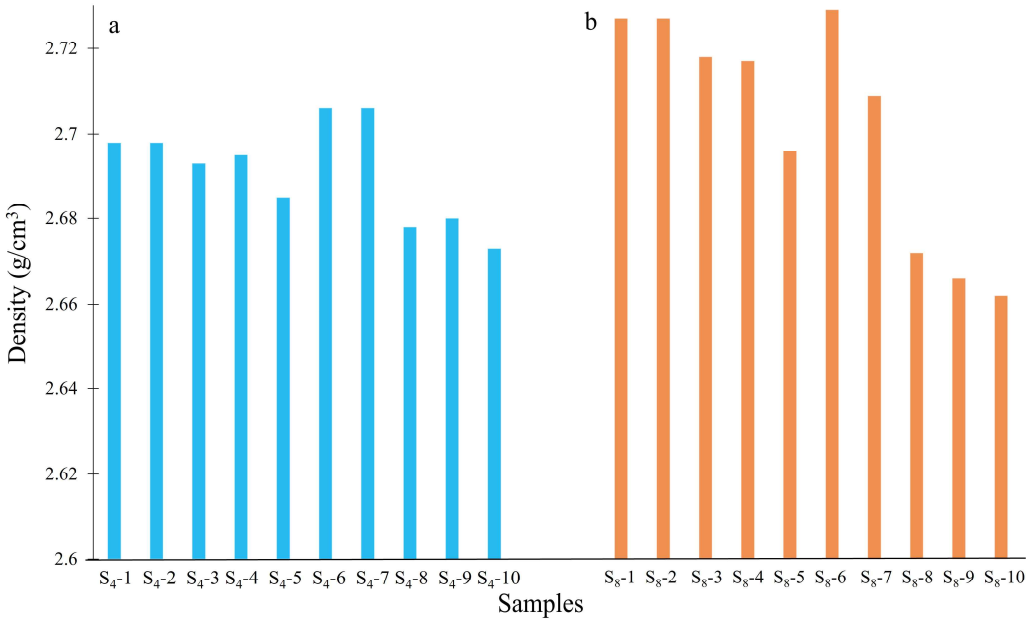

Figure 18. Density results of samples S_4-1 to S_4-10 (a) and S_8-1 to S_8-10 (b)

When analyzing the side surfaces of samples microscopically, similar tendency of porosity increase was observed, when the E_v>98 J/mm^3, as shown in Figures 19 and 20. This denotes, that increase in E_v to a certain extent results to surface defects and porosities. Maximum density values were measured for samples S_4-6 and S_8-6, when applied E_v=89.7J/mm^3. According to the image analysis of these samples, the estimated porosity reaches to 0.37±0.23% for S_4-6 and 0.68±0.19% for S_8-6 samples.

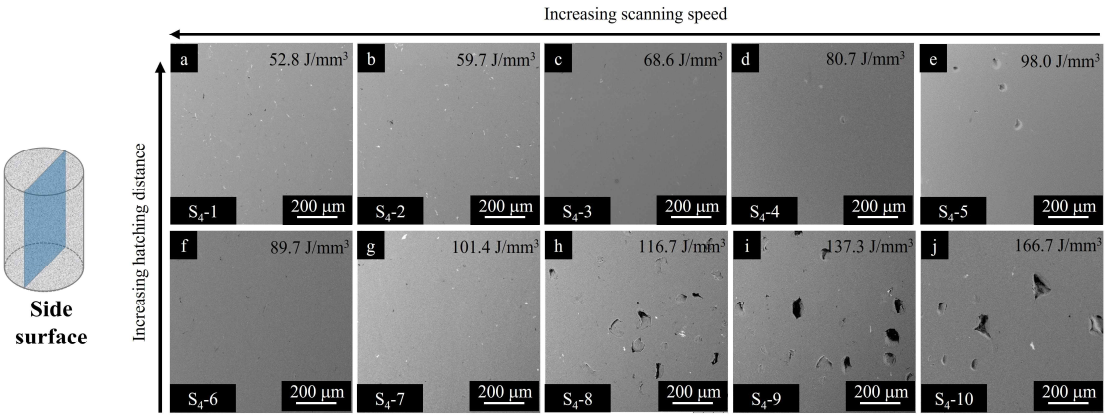

Figure 19. Side surface SEM images of SLM processed AlSi10Mg/4 wt.%(Ti+BN) samples.

In case of SLMed AlSi10Mg/4wt.%(Ti+hBN) system, very few pores are detected at S_4-1-4 (Fig. 19 a-d) and S_4-6 samples (Fig. 19f), however, the decrease in scanning speed results in gradual increase in porosity in the rows. The pores at higher energy density may arise by significant local overheating leading to material evaporation during the laser scanning, resulting keyhole pores [91].

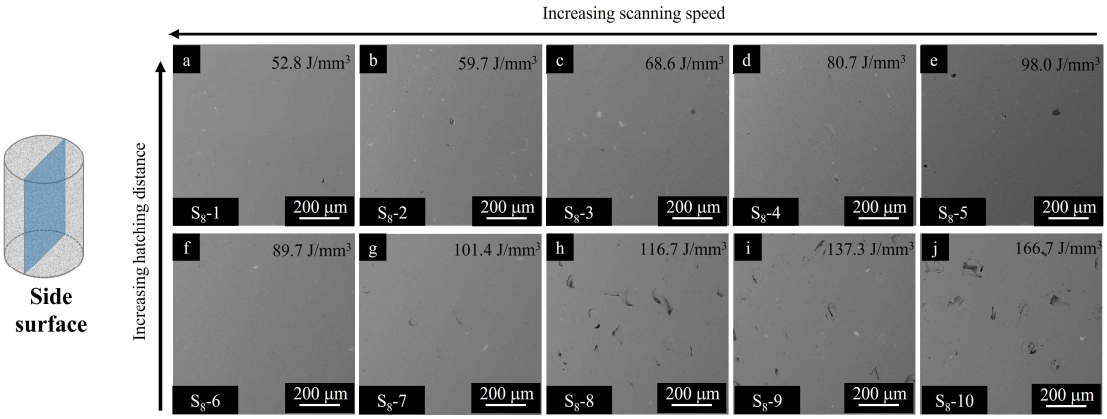

Figure 20. Side surface SEM images of SLM proceesed AlSi10Mg/8 wt.%(Ti+BN) samples.

The porosity trend in SLM prepared AlSi10Mg/8wt.%(Ti+BN) system is similar to that of AlSi10Mg/4wt.%(Ti+BN), however, the size of pores in the S_8-8-10 is significantly smaller. One possibility is that in-situ formed TiB_2 and TiN phases interfere with porosity formation. The melting points of TiB_2 and TiN are 3230℃ and 2950℃ [92], [93], respectively, compared to the relatively lower melting point of AlSi10Mg (660℃). TiB_2 and TiN with high refractory suppress the expanding gas vaporization, leading to inhibiting the formation of pores [94].

In all three XRD patterns, the peaks corresponding to the face-centered cubic (FCC) α-Al and diamond-like cubic Si phases are present. In-situ formed $Ti_{0.83}N_{0.17}$, TiB_2, $Al_{2.55}Si_{0.45}Ti$ and Al_3Ti phases are observed in the S_4-6 and S_8-6 samples, as a result of Al-Ti, Al-Si-Ti, Ti+hBN interactions.

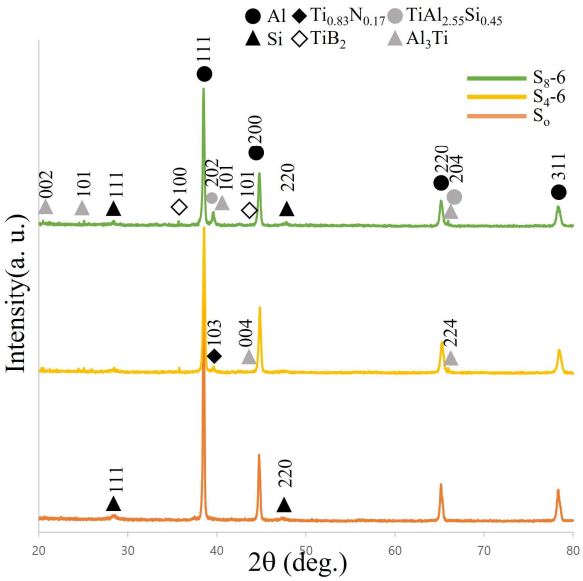

Figure 21. X-ray diffractograms of S_0, S_4, S_8 samples.

When microscopically analyzing the samples at higher magnifications, in-situ formed phases and unreacted hBN microflakes are visible in SEM images of S_4-6 and S_8-6 (Fig. 22b-f). According to EDS analysis results (Area 1, Fig. 22g, h), the white features observed on reinforced S_4-6 sample, are composed of Al, Si and Ti, which is in match with XRD results stating the formation of Al_3Ti and $Al_{2.55}Si_{0.45}Ti$ phases. However, no titanium was detected in Area 2 (Fig 22i, k and p). The dark gray features observed in Fig. 22j represents unreacted hexagonal boron nitride phase by, as shown in Fig. 22j. The hBN particles were completely wetted by the Al-Si-Ti melt, because no cracking, detachment or delamination was observed at the hBN/Al interfaces.

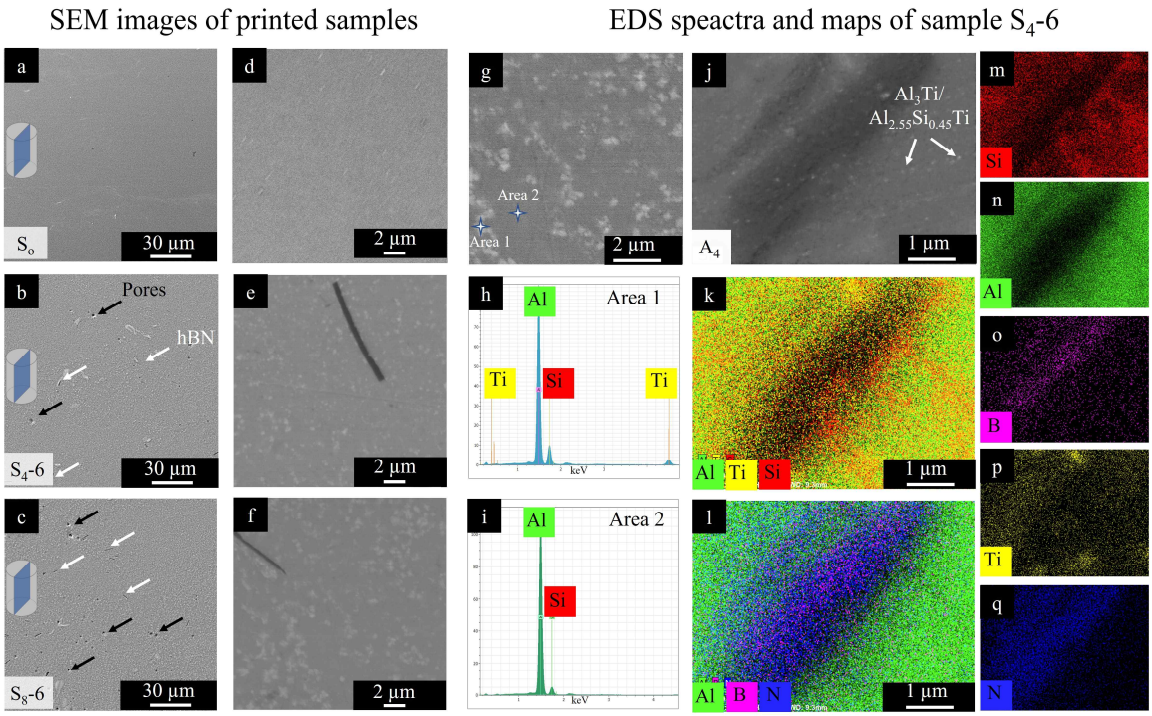

Figure 22. SEM images of polished S_0 (a), S_4-6 (b), S_8-6(c). High magnification SEM images of S_0 (d), S_4-6 (e), S_8-6. SEM image (g) and EDS Spectra of S_4-6 sample (h, i). High magnification SEM image (j) and EDS maps of S_4-6 sample(k-q).

The in-situ formed intermetalics are in tens of nanometers to less than 1 micrometer range and are known to have coherent interface with Al matrix and can serve as efficient heterogeneous nucleation cites and hence grain refiners [95]. The microstructure of melt pool of side and top surface for SLM-fabricated AlSi10Mg and reinforced AMCs are shown in Fig. 22a-f.

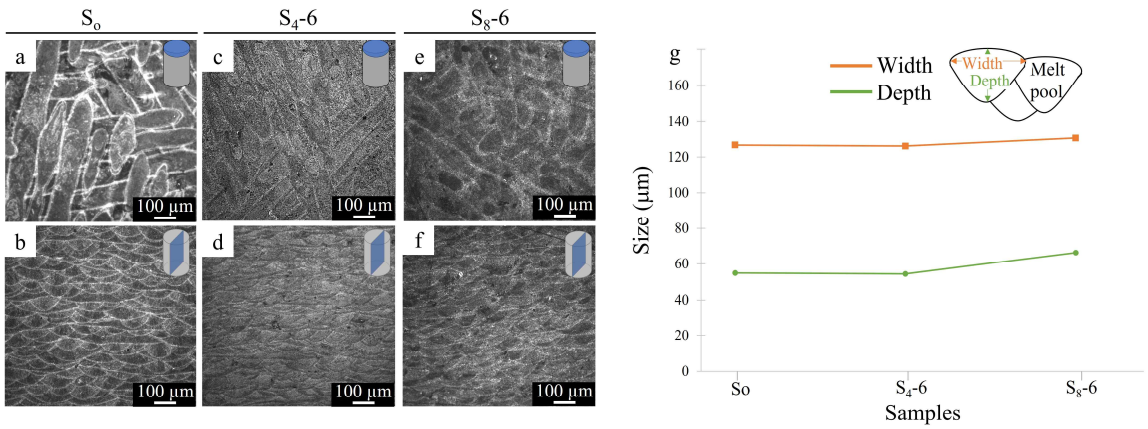

Figure 23. Etched optical microscope images. Top (a) and side (b) surface of S_0, top (c) and side (d) surface of S_4-6, top (c), side (f) surface of S_8-6 and the dimension of melt pool of side surface (g).

The melt pools of AlSi10Mg reinforced with 4 wt.% (Ti+hBN) additive have a width average of 126 μm and a depth of 54.4 μm, showing no significant difference in comparison with AlSi10Mg with 126.6 μm width and 54.8 μm depth respectively in melt pool dimension. However, in the case of AMC reinforced with 8 wt.% (Ti+hBN) additive, the average width and depth of the melt pool increased to 130.4 μm and 66.2 μm. The reason might be the improved laser absorptivity of the blended mixture and the exothermic chemical reactions rising the temperature of the melting pool, which decreases the viscosity of the liquid phase leading to increase in melt pool dimensions.

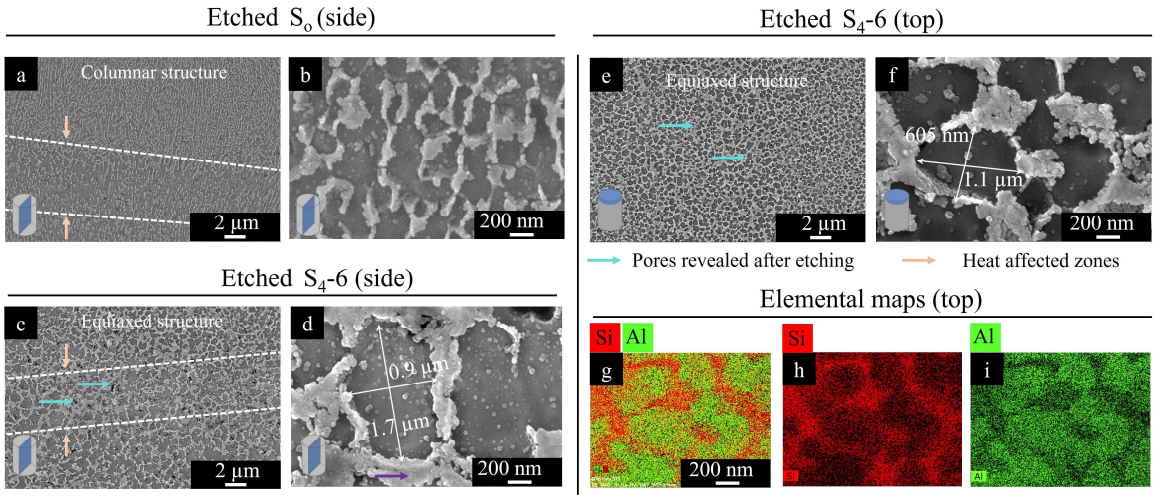

Figure 24. SEM images of etched longitudinal cross sections of samples S_o (a, b) and S_4-6 (c, d), SEM images of transverse cross section of sample S_4-6 (g, h) and top surface EDS elemental maps (g, h, i) of (f).

When analyzing the etched S_o sample, it was revealed, that α-Al cells are surrounded by a eutectic Si network as shown in Fig. 24a, b. Meanwhile, uniformly distributed spherical Si nanoparticles are observed in α-Al cells. The area marked with orange colored arrows shows a discontinuous Si network in the heat-affected zones (HAZ). In S_o columnar fine α-Al cells have been grown epitaxially along the build direction.

In S_4-6 sample the Al cells have equiaxed morphology. The Si network is reltiveley continuous both on top and side surfaces of the S_4-6 sample (Fig. 24c-i). Meanwhile, the α-Al cells are finer on the transversal cross-section, being in 0.5-1 μm range (Fig. 24e and f). The columnar to equiaxed transofromation of the α-Al cells when adding Ti-hBN additive, states that the in-situ formed TiN_x, TiB_2, Al_3Ti, $Al_{2.55}Si_{0.45}Ti$ phases served as grain refiners and reduced the grain size, hence decreasing the crystallographic texturing and anisotropy in mechanical properties.

a

SLM prepared AlSi10Mg+4wt.% (Ti+BN)		SLM prepared AlSi10Mg+8wt.% (Ti+BN)	
Sample number	Vicker's Hardness (HV1)	Sample number	Vicker's Hardness (HV1)
S_4-1	142.1±1.0	S_8-1	158.4±4.7
S_4-2	139.7±2.0	S_8-2	160.1±1.7
S_4-3	136.6±0.2	S_8-3	155.7±3.1
S_4-4	137.6±3.5	S_8-4	156.9±7.6
S_4-5	135.3±0.1	S_8-5	151.6±5.4
S_4-6	141.6±3.5	S_8-6	160.8±1.7
S_4-7	149.3±1.5	S_8-7	158.6±3.0
S_4-8	141.9±7.2	S_8-8	151.9±4.4
S_4-9	138.9±3.0	S_8-9	149.3±0.4
S_4-10	132.9±3.1	S_8-10	146.7±1.3

b

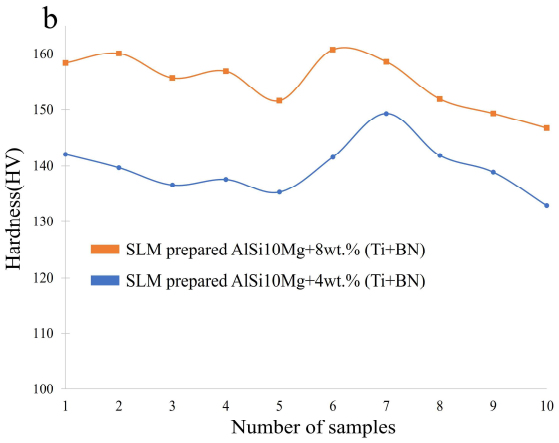

Figure 25. The Vicker's hardness values for S_4-1 to S_4-10 and S_8-1 to S_8-10 samples (a), and the hardness chart for comparison (b).

The measured Vicker's hardness values of the composites are remarkably higher than that of the AlSi10Mg alloy (S_o) (115 HV1) with an average of 139.59 HV1 and 155 HV1 of SLM prepared AlSi10Mg/4wt.%(Ti+hBN) and AlSi10Mg/8 wt.%(Ti+hBN), respectively, due to the hardening effect of in-situ formed TiB_2 and TiN_x reinforcements, as well as the refined microstructure. As shown in Fig. 25a and 25b, overall, the hardness of SLM prepared AlSi10Mg/8wt.%(Ti+hBN) is higher than that of 4%(Ti+hBN). S_8-6 has the highest hardness of 160.8HV.

4 SUMMARY

In this work, AlSi10Mg powder with (Ti-hBN) additive mixture was consolidated via selective laser melting process. The influence of the in-situ formed reinforcing compounds on the microstructure and mechanical properties of aluminium matrix composite bulks was investigated. Prior to experimental stage, thermodynamic calculations were performed to study the possible chemical reactions within the Al-Si-Ti-BN system. Two different content of additive mixtures was used, mainly 4wt.% and 8wt.%(Ti+hBN) and set of experiments were performed to find the optimal process window for SLM consolidation.

Below are the main highlights of the work.

Negligible porosity was observed in both SLM prepared AlSi10Mg/4 and 8wt.% (Ti+hBN) samples, when applied volumetric energy density (E_v) was in 52-89J/mm^3 range, however above this value porosity was observed.

Al_3Ti and $Al_{(3-x)}Si_xTi$ nanoparticles were formed in-situ in Ti-rich Al-Si liquid and have been known provide highly coherent interfaces with Al and serve as a potential grain refiners. TiB_2, TiN_x phases were formed during reactive sintering process owing to Ti-hBN reaction.

The measured Vicker's hardness for composites is remarkably higher than that of the unreinforced AlSi10Mg alloys (115 HV_1) with an average of 139.59 HV_1 and 155 HV1 of SLM fabricated AlSi10Mg/4 wt.%(Ti+hBN) and AlSi10Mg 8 wt.%(Ti+hBN), respectively, due to the hardening effect of in-situ formed TiB_2 and TiN_x reinforcements and refined microstructure.

In SLM prepared AlSi10Mg/4 and 8wt.% (Ti+hBN) samples the columnar α-Al cells were almost completely transformed to equiaxed, as compared to unreinforced AlSi10Mg counterparts, owing to the efficient grain refining influence of the newly formed phases.

Kokkuvõte

Selles töös tugevdati selektiivse lasersulatusprotsessi abil pulber AlSi10Mg koos lisandainega Ti-hBN. Uuriti in situ protsessis moodustunud tugevdavate ühendite mõju alumiiniummaatriks komposiit katsekehade mikrostruktuurile ja mehaanilistele omadustele. Enne eksperimentaalosa tehti termodünaamilised arvutused, et uurida erinevate võimalikke keemiliste ühendite tekkimist Al-Si-Ti-BN süsteemis. AlSi10Mg pulbrisse lisati kahe erineva massiprotsendiga sama lisaainet, 4wt.% ja 8wt.%(Ti+hBN). Läbi viidud katsetes kasutati ainult SLM protsessi. Protsessi käigus muudeti parameetrid, et leida konsolideerimiseks kõige optimaalsem viis komposiidi valmistamiseks.

Allpool on välja toodud töö tähtsamad tulemused.

Poorsust uuriti mõlema AlSi10Mg/4 ja 8wt.% (Ti+hBN) katsekeha puhul, kui mahuline energiatihedus jäi vahemikku 52-89J/mm^3, ei pööratud sellele erilist tähelepanu. Kuid väärtused, mis ületasid 89J/mm^3 võeti arvesse ning uuriti lähemalt.

Al_3Ti and $Al_{(3-x)}Si_xTi$ nanoosakesed moodustati in-situ Ti-rikkas Al-Si vedela faasi keskkonnas, mis kirjandusest teadaolevalt moodustab väga hea piirpindade nakkumise alumiiniumi ning titaaniumi vahel ning samuti toimivad potentsiaalsete teradepeenendajatena, TiB_2, TiN_x faasid moodustati reaktiivse paagutamisprotsessi käigus, mis põhinevad Ti-hBN reaktsioonil.

Valmistatud Komposiitide Vickeri kõvadus on märkimisväärselt kõrgem kui tugevdamata AlSi10Mg sulamitel (115 HV_1), mille keskmine kõvadus osutus olema 139.59 HV_1 ja 155 HV_1. SLM protsessi põhjal valmistatud AlSi10Mg/4 ja 8 wt.% (Ti+hBN), vastavalt in-situ moodustunud TiB_2 ja TiN_x tugevduste ning rafineeritud mikrostruktuuri kõveneva toime tõttu.

SLM protsessiga valmistatud AlSi10Mg/4 ja 8wt.% (Ti+hBN) katsekehades transformeerusid sambakujulised α-Al faasi kristallid peaaegu täielikult võrdtelgkristallstruktuurile ümber. Võrreldes tugevdamata AlSi10Mg ühendiga, kus kristalli faasi muundumist ei toimunud. Põhjuseks saab välja tuua ühendite piirpindade vahelise tõhusa nakkumise tõttu.

LIST OF REFERENCES

[1] C. Kammer, “Aluminium-Verlag Marketing & Kommunikation GmbH, Germany,” in *Aluminium Handbook*, vol. 61–73, 1999.

[2] J. Zhang, B. Song, Q. Wei, D. Bourell, and Y. Shi, “A review of selective laser melting of aluminum alloys: Processing, microstructure, property and developing trends,” *Journal of Materials Science & Technology*, vol. 35, no. 2, pp. 270–284, Feb. 2019, doi: 10.1016/j.jmst.2018.09.004.

[3] X. Cao, W. Wallace, C. Poon, and J.-P. Immarigeon, “Research and Progress in Laser Welding of Wrought Aluminum Alloys. I. Laser Welding Processes,” *Materials and Manufacturing Processes*, vol. 18, no. 1, pp. 1–22, Jan. 2003, doi: 10.1081/AMP-120017586.

[4] D. Herzog, V. Seyda, E. Wycisk, and C. Emmelmann, “Additive manufacturing of metals,” *Acta Materialia*, vol. 117, pp. 371–392, Sep. 2016, doi: 10.1016/j.actamat.2016.07.019.

[5] S. A. Jawade, Rashmi. S. Joshi, and S. B. Desai, “Comparative study of mechanical properties of additively manufactured aluminum alloy,” *Materials Today: Proceedings*, vol. 46, pp. 9270–9274, 2021, doi: 10.1016/j.matpr.2020.02.096.

[6] A. Vafadar, F. Guzzomi, A. Rassau, and K. Hayward, “Advances in Metal Additive Manufacturing: A Review of Common Processes, Industrial Applications, and Current Challenges,” *Applied Sciences*, vol. 11, no. 3, p. 1213, Jan. 2021, doi: 10.3390/app11031213.

[7] J.-Y. Lee, A. P. Nagalingam, and S. H. Yeo, “A review on the state-of-the-art of surface finishing processes and related ISO/ASTM standards for metal additive manufactured components,” *Virtual and Physical Prototyping*, vol. 16, no. 1, pp. 68–96, Jan. 2021, doi: 10.1080/17452759.2020.1830346.

[8] J. Jiang, S. T. Newman, and R. Y. Zhong, “A review of multiple degrees of freedom for additive manufacturing machines,” *International Journal of Computer Integrated Manufacturing*, vol. 34, no. 2, pp. 195–211, Feb. 2021, doi: 10.1080/0951192X.2020.1858510.

[9] T. D. Ngo, A. Kashani, G. Imbalzano, K. T. Q. Nguyen, and D. Hui, “Additive manufacturing (3D printing): A review of materials, methods, applications and challenges,” *Composites Part B: Engineering*, vol. 143, pp. 172–196, Jun. 2018, doi: 10.1016/j.compositesb.2018.02.012.

[10] P. Stavropoulos and P. Foteinopoulos, “Modelling of additive manufacturing processes: a review and classification,” *Manufacturing Review*, vol. 5, p. 2, Mar. 2018, doi: 10.1051/mfreview/2017014.

[11] M. Bhuvanesh Kumar and P. Sathiya, “Methods and materials for additive manufacturing: A critical review on advancements and challenges,” *Thin-Walled Structures*, vol. 159, p. 107228, Feb. 2021, doi: 10.1016/j.tws.2020.107228.

[12] S. C. Daminabo, S. Goel, S. A. Grammatikos, H. Y. Nezhad, and V. K. Thakur, “Fused deposition modeling-based additive manufacturing (3D printing): techniques for polymer material systems,” *Materials Today Chemistry*, vol. 16, p. 100248, Jun. 2020, doi: 10.1016/j.mtchem.2020.100248.

[13] J. Ni *et al.*, “Three-dimensional printing of metals for biomedical applications,” *Materials Today Bio*, vol. 3, p. 100024, Jun. 2019, doi: 10.1016/j.mtbio.2019.100024.

[14] B. Nagarajan, Z. Hu, X. Song, W. Zhai, and J. Wei, “Development of Micro Selective Laser Melting: The State of the Art and Future Perspectives,” *Engineering*, vol. 5, no. 4, pp. 702–720, Aug. 2019, doi: 10.1016/j.eng.2019.07.002.
[15] S. Bremen, W. Meiners, and A. Diatlov, “Selective Laser Melting,” *Laser Technik Journal*, vol. 9, no. 2, pp. 33–38, Apr. 2012, doi: 10.1002/latj.201290018.
[16] L.-E. Loh *et al.*, “Numerical investigation and an effective modelling on the Selective Laser Melting (SLM) process with aluminium alloy 6061,” *International Journal of Heat and Mass Transfer*, vol. 80, pp. 288–300, Jan. 2015, doi: 10.1016/j.ijheatmasstransfer.2014.09.014.
[17] T. Minasyan, “MoSi2-based Composites by Selective Laser Melting,” 2020.
[18] S. Giganto, P. Zapico, M. Á. Castro-Sastre, S. Martínez-Pellitero, P. Leo, and P. Perulli, “Influence of the scanning strategy parameters upon the quality of the SLM parts,” *Procedia Manufacturing*, vol. 41, pp. 698–705, 2019, doi: 10.1016/j.promfg.2019.09.060.
[19] R. Baitimerov, P. Lykov, D. Zherebtsov, L. Radionova, A. Shultc, and K. Prashanth, “Influence of Powder Characteristics on Processability of AlSi12 Alloy Fabricated by Selective Laser Melting,” *Materials*, vol. 11, no. 5, p. 742, May 2018, doi: 10.3390/ma11050742.
[20] B. Meier *et al.*, “Effect of the reuse of powder on material properties of Ti6Al4V processed by SLM,” 2019, p. 150006. doi: 10.1063/1.5112682.
[21] R. Mertens, S. Dadbakhsh, J. van Humbeeck, and J.-P. Kruth, “Application of base plate preheating during selective laser melting,” *Procedia CIRP*, vol. 74, pp. 5–11, 2018, doi: 10.1016/j.procir.2018.08.002.
[22] A. bin Anwar and Q.-C. Pham, “Selective laser melting of AlSi10Mg: Effects of scan direction, part placement and inert gas flow velocity on tensile strength,” *Journal of Materials Processing Technology*, vol. 240, pp. 388–396, Feb. 2017, doi: 10.1016/j.jmatprotec.2016.10.015.
[23] J. Kruth, P. Mercelis, J. van Vaerenbergh, L. Froyen, and M. Rombouts, “Binding mechanisms in selective laser sintering and selective laser melting,” *Rapid Prototyping Journal*, vol. 11, no. 1, pp. 26–36, Feb. 2005, doi: 10.1108/13552540510573365.
[24] www.slm-solutions.com., “SLM Solutions GmbH.”
[25] M. Aghayan and I. Hussainova, “Fabrication of NiO/NiAl₂O₄ Nanofibers by Combustion Method,” *Key Engineering Materials*, vol. 674, pp. 31–34, Jan. 2016, doi: 10.4028/www.scientific.net/KEM.674.31.
[26] Standard Test Methods of Compression Testing of Metallic Materials at Room Temperature, “ASTM E9-09,” 2009.
[27] Lipson Hod and Melba Kurman., *Fabricated: The new world of 3D printing.* . John Wiley & Sons, 2013.
[28] I. Yadroitsev and I. Smurov, “Surface Morphology in Selective Laser Melting of Metal Powders,” *Physics Procedia*, vol. 12, pp. 264–270, 2011, doi: 10.1016/j.phpro.2011.03.034.
[29] J. Zhang, B. Song, Q. Wei, D. Bourell, and Y. Shi, “A review of selective laser melting of aluminum alloys: Processing, microstructure, property and developing trends,” *Journal of Materials Science & Technology*, vol. 35, no. 2, pp. 270–284, Feb. 2019, doi: 10.1016/J.JMST.2018.09.004.

[30] A. Plotkowski *et al.*, “Microstructure and properties of a high temperature Al–Ce–Mn alloy produced by additive manufacturing,” *Acta Materialia*, vol. 196, pp. 595–608, Sep. 2020, doi: 10.1016/J.ACTAMAT.2020.07.014.
[31] M. Wang, B. Song, Q. Wei, and Y. Shi, “Improved mechanical properties of AlSi7Mg/nano-SiCp composites fabricated by selective laser melting,” *Journal of Alloys and Compounds*, vol. 810, p. 151926, Nov. 2019, doi: 10.1016/J.JALLCOM.2019.151926.
[32] P. Li *et al.*, “Selective laser melting of Al-3.48Cu-2.03Si-0.48Sc-0.28Zr alloy: Microstructure evolution, properties and metallurgical defects,” *Intermetallics (Barking)*, vol. 129, p. 107008, Feb. 2021, doi: 10.1016/J.INTERMET.2020.107008.
[33] Z. Fan *et al.*, “In situ formation of D022-Al3Ti during selective laser melting of nano-TiC/AlSi10Mg alloy prepared by electrostatic self-assembly,” *Vacuum*, vol. 188, p. 110179, Jun. 2021, doi: 10.1016/J.VACUUM.2021.110179.
[34] J. Gilbert Kaufman, *Introduction to Aluminum Alloys and Tempers* . Google Books.
[35] M. L. Montero-Sistiaga *et al.*, “Changing the alloy composition of Al7075 for better processability by selective laser melting,” *Journal of Materials Processing Technology*, vol. 238, pp. 437–445, Dec. 2016, doi: 10.1016/j.jmatprotec.2016.08.003.
[36] L. C. Astfalck, G. K. Kelly, X. Li, and T. B. Sercombe, “On the Breakdown of SiC during the Selective Laser Melting of Aluminum Matrix Composites ,” *Advanced Engineering Materials*, vol. 19, no. 8, p. 1600835, Aug. 2017, doi: 10.1002/adem.201600835.
[37] X. P. Li *et al.*, “A selective laser melting and solution heat treatment refined Al–12Si alloy with a controllable ultrafine eutectic microstructure and 25% tensile ductility,” *Acta Materialia*, vol. 95, pp. 74–82, Aug. 2015, doi: 10.1016/j.actamat.2015.05.017.
[38] L. Zhuo *et al.*, “Effect of post-process heat treatment on microstructure and properties of selective laser melted AlSi10Mg alloy,” *Materials Letters*, vol. 234, pp. 196–200, Jan. 2019, doi: 10.1016/j.matlet.2018.09.109.
[39] B. Chen, X. Xi, C. Tan, and X. Song, “Recent progress in laser additive manufacturing of aluminum matrix composites,” *Current Opinion in Chemical Engineering*, vol. 28, pp. 28–35, Jun. 2020, doi: 10.1016/j.coche.2020.01.005.
[40] B. Chen *et al.*, “Length effect of carbon nanotubes on the strengthening mechanisms in metal matrix composites,” *Acta Materialia*, vol. 140, pp. 317–325, Nov. 2017, doi: 10.1016/j.actamat.2017.08.048.
[41] J. Li, J. Nie, Q. Xu, K. Zhao, and X. Liu, “Enhanced mechanical properties of a novel heat resistant Al-based composite reinforced by the combination of nano-aluminides and submicron TiN particles,” *Materials Science and Engineering: A*, vol. 770, p. 138488, Jan. 2020, doi: 10.1016/j.msea.2019.138488.
[42] L.-Y. Chen *et al.*, “Processing and properties of magnesium containing a dense uniform dispersion of nanoparticles,” *Nature*, vol. 528, no. 7583, pp. 539–543, Dec. 2015, doi: 10.1038/nature16445.
[43] N. K. Babu, K. Kallip, M. Leparoux, K. A. AlOgab, X. Maeder, and Y. A. R. Dasilva, “Influence of microstructure and strengthening mechanism of AlMg5–Al 2 O 3 nanocomposites prepared via spark plasma sintering,” *Materials & Design*, vol. 95, pp. 534–544, Apr. 2016, doi: 10.1016/j.matdes.2016.01.138.
[44] I. M. Kusoglu, B. Gökce, and S. Barcikowski, “Use of (nano-)additives in Laser Powder Bed Fusion of Al powder feedstocks: research directions within the last

decade," *Procedia CIRP*, vol. 94, pp. 11–16, Jan. 2020, doi: 10.1016/J.PROCIR.2020.09.003.
[45] O. H. Famodimu, M. Stanford, C. F. Oduoza, and L. Zhang, "Effect of process parameters on the density and porosity of laser melted AlSi10Mg/SiC metal matrix composite," *Frontiers of Mechanical Engineering 2018 13:4*, vol. 13, no. 4, pp. 520–527, Jun. 2018, doi: 10.1007/S11465-018-0521-Y.
[46] D. Gu, Y. Yang, L. Xi, J. Yang, and M. Xia, "Laser absorption behavior of randomly packed powder-bed during selective laser melting of SiC and TiB2 reinforced Al matrix composites," *Optics & Laser Technology*, vol. 119, p. 105600, Nov. 2019, doi: 10.1016/j.optlastec.2019.105600.
[47] L. Xi *et al.*, "Effect of TiB2 particles on microstructure and crystallographic texture of Al-12Si fabricated by selective laser melting," *Journal of Alloys and Compounds*, vol. 786, pp. 551–556, May 2019, doi: 10.1016/J.JALLCOM.2019.01.327.
[48] Q. Tan *et al.*, "A novel method to 3D-print fine-grained AlSi10Mg alloy with isotropic properties via inoculation with LaB6 nanoparticles," *Additive Manufacturing*, vol. 32, p. 101034, Mar. 2020, doi: 10.1016/J.ADDMA.2019.101034.
[49] X. Li, G. Li, M.-X. Zhang, and Q. Zhu, "Novel approach to additively manufacture high-strength Al alloys by laser powder bed fusion through addition of hybrid grain refiners," *Additive Manufacturing*, p. 102400, Oct. 2021, doi: 10.1016/j.addma.2021.102400.
[50] Y. Liu *et al.*, "Microstructural evolution and mechanical performance of in-situ TiB2/AlSi10Mg composite manufactured by selective laser melting," *Journal of Alloys and Compounds*, vol. 853, p. 157287, Feb. 2021, doi: 10.1016/j.jallcom.2020.157287.
[51] Z. Fan *et al.*, "In situ formation of D022-Al3Ti during selective laser melting of nano-TiC/AlSi10Mg alloy prepared by electrostatic self-assembly," *Vacuum*, vol. 188, p. 110179, Jun. 2021, doi: 10.1016/j.vacuum.2021.110179.
[52] C. Gao, Z. Wang, Z. Xiao, D. You, K. Wong, and A. H. Akbarzadeh, "Selective laser melting of TiN nanoparticle-reinforced AlSi10Mg composite: Microstructural, interfacial, and mechanical properties," *Journal of Materials Processing Technology*, vol. 281, p. 116618, Jul. 2020, doi: 10.1016/j.jmatprotec.2020.116618.
[53] C. Gao, W. Wu, J. Shi, Z. Xiao, and A. H. Akbarzadeh, "Simultaneous enhancement of strength, ductility, and hardness of TiN/AlSi10Mg nanocomposites via selective laser melting," *Additive Manufacturing*, vol. 34, p. 101378, Aug. 2020, doi: 10.1016/j.addma.2020.101378.
[54] M. Wang, B. Song, Q. Wei, and Y. Shi, "Improved mechanical properties of AlSi7Mg/nano-SiCp composites fabricated by selective laser melting," *Journal of Alloys and Compounds*, vol. 810, p. 151926, Nov. 2019, doi: 10.1016/j.jallcom.2019.151926.
[55] X. Nie, H. Zhang, H. Zhu, Z. Hu, L. Ke, and X. Zeng, "Effect of Zr content on formability, microstructure and mechanical properties of selective laser melted Zr modified Al-4.24Cu-1.97Mg-0.56Mn alloys," *Journal of Alloys and Compounds*, vol. 764, pp. 977–986, Oct. 2018, doi: 10.1016/j.jallcom.2018.06.032.
[56] Y. K. Xiao *et al.*, "Effect of nano-TiB2 particles on the anisotropy in an AlSi10Mg alloy processed by selective laser melting," *Journal of Alloys and Compounds*, vol. 798, pp. 644–655, Aug. 2019, doi: 10.1016/j.jallcom.2019.05.279.

[57] Q. Tan, Y. Yin, Z. Fan, J. Zhang, Y. Liu, and M.-X. Zhang, “Uncovering the roles of LaB6-nanoparticle inoculant in the AlSi10Mg alloy fabricated via selective laser melting,” *Materials Science and Engineering: A*, vol. 800, p. 140365, Jan. 2021, doi: 10.1016/j.msea.2020.140365.

[58] W. Cheng, Y. Liu, X. Xiao, B. Huang, Z. Zhou, and X. Liu, “Microstructure and mechanical properties of a novel (TiB2+TiC)/AlSi10Mg composite prepared by selective laser melting,” *Materials Science and Engineering: A*, vol. 834, p. 142435, Feb. 2022, doi: 10.1016/j.msea.2021.142435.

[59] M. Wang, B. Song, Q. Wei, and Y. Shi, “Improved mechanical properties of AlSi7Mg/nano-SiCp composites fabricated by selective laser melting,” *Journal of Alloys and Compounds*, vol. 810, p. 151926, Nov. 2019, doi: 10.1016/j.jallcom.2019.151926.

[60] D. Dai *et al.*, “Melt spreading behavior, microstructure evolution and wear resistance of selective laser melting additive manufactured AlN/AlSi10Mg nanocomposite,” *Surface and Coatings Technology*, vol. 349, pp. 279–288, Sep. 2018, doi: 10.1016/j.surfcoat.2018.05.072.

[61] A. S. Konopatsky *et al.*, “Microstructure evolution during AlSi10Mg molten alloy/BN microflake interactions in metal matrix composites obtained through 3D printing,” *Journal of Alloys and Compounds*, vol. 859, p. 157765, Apr. 2021, doi: 10.1016/j.jallcom.2020.157765.

[62] X. Liu, Y. Liu, Z. Zhou, K. Wang, Q. Zhan, and X. Xiao, “Grain refinement and crack inhibition of selective laser melted AA2024 aluminum alloy via inoculation with TiC–TiH2,” *Materials Science and Engineering: A*, vol. 813, p. 141171, May 2021, doi: 10.1016/j.msea.2021.141171.

[63] B. H. al khaqani, “Reviews on effect of Additions the alloying element on the Microstructure and Mechanical Properties of Aluminum Alloys,” *International Journal of Engineering and Technology*, vol. 12, no. 2, pp. 155–159, Apr. 2020, doi: 10.21817/ijet/2020/v12i2/201202027.

[64] N. Kang, P. Coddet, L. Dembinski, H. Liao, and C. Coddet, “Microstructure and strength analysis of eutectic Al-Si alloy in-situ manufactured using selective laser melting from elemental powder mixture,” *Journal of Alloys and Compounds*, vol. 691, pp. 316–322, Jan. 2017, doi: 10.1016/j.jallcom.2016.08.249.

[65] Y. Shi, P. Rometsch, K. Yang, F. Palm, and X. Wu, “Characterisation of a novel Sc and Zr modified Al–Mg alloy fabricated by selective laser melting,” *Materials Letters*, vol. 196, pp. 347–350, Jun. 2017, doi: 10.1016/j.matlet.2017.03.089.

[66] P. Wang, H. C. Li, K. G. Prashanth, J. Eckert, and S. Scudino, “Selective laser melting of Al-Zn-Mg-Cu: Heat treatment, microstructure and mechanical properties,” *Journal of Alloys and Compounds*, vol. 707, pp. 287–290, Jun. 2017, doi: 10.1016/j.jallcom.2016.11.210.

[67] J. A. Glerum, C. Kenel, T. Sun, and D. C. Dunand, “Synthesis of precipitation-strengthened Al-Sc, Al-Zr and Al-Sc-Zr alloys via selective laser melting of elemental powder blends,” *Additive Manufacturing*, vol. 36, p. 101461, Dec. 2020, doi: 10.1016/j.addma.2020.101461.

[68] L. Yan *et al.*, “Effect of Zn addition on microstructure and mechanical properties of an Al–Mg–Si alloy,” *Progress in Natural Science: Materials International*, vol. 24, no. 2, pp. 97–100, Apr. 2014, doi: 10.1016/j.pnsc.2014.03.003.

[69] P. Wang, L. Deng, K. G. Prashanth, S. Pauly, J. Eckert, and S. Scudino, “Microstructure and mechanical properties of Al-Cu alloys fabricated by selective laser melting of powder mixtures,” *Journal of Alloys and Compounds*, vol. 735, pp. 2263–2266, Feb. 2018, doi: 10.1016/j.jallcom.2017.10.168.

[70] D. R. Manca *et al.*, “Microstructure and Properties of Novel Heat Resistant Al–Ce–Cu Alloy for Additive Manufacturing,” *Metals and Materials International*, vol. 25, no. 3, pp. 633–640, May 2019, doi: 10.1007/s12540-018-00211-0.
[71] J. Lu, X. Lin, N. Kang, Y. Cao, Q. Wang, and W. Huang, “Keyhole mode induced simultaneous improvement in strength and ductility of Sc modified Al–Mn alloy manufactured by selective laser melting,” *Materials Science and Engineering: A*, vol. 811, p. 141089, Apr. 2021, doi: 10.1016/j.msea.2021.141089.
[72] S. Yamasaki, T. Okuhira, M. Mitsuhara, H. Nakashima, J. Kusui, and M. Adachi, “Effect of Fe Addition on Heat-Resistant Aluminum Alloys Produced by Selective Laser Melting,” *Metals (Basel)*, vol. 9, no. 4, p. 468, Apr. 2019, doi: 10.3390/met9040468.
[73] A. G. Demir and B. Previtali, “Multi-material selective laser melting of Fe/Al-12Si components,” *Manufacturing Letters*, vol. 11, pp. 8–11, Jan. 2017, doi: 10.1016/j.mfglet.2017.01.002.
[74] N. Kang *et al.*, “In-situ synthesis of aluminum/nano-quasicrystalline Al-Fe-Cr composite by using selective laser melting,” *Composites Part B: Engineering*, vol. 155, pp. 382–390, Dec. 2018, doi: 10.1016/j.compositesb.2018.08.108.
[75] T. Minasyan and I. Hussainova, “Laser Powder-Bed Fusion of Ceramic Particulate Reinforced Aluminum Alloys: A Review,” *Materials*, vol. 15, no. 7, p. 2467, Mar. 2022, doi: 10.3390/ma15072467.
[76] N. Kang *et al.*, “In-situ synthesis of aluminum/nano-quasicrystalline Al-Fe-Cr composite by using selective laser melting,” *Composites Part B: Engineering*, vol. 155, pp. 382–390, Dec. 2018, doi: 10.1016/j.compositesb.2018.08.108.
[77] A. Wang *et al.*, “Characterisation of the multiple effects of Sc/Zr elements in selective laser melted Al alloy,” *Materials Characterization*, vol. 183, p. 111653, Jan. 2022, doi: 10.1016/j.matchar.2021.111653.
[78] M. L. Montero-Sistiaga *et al.*, “Changing the alloy composition of Al7075 for better processability by selective laser melting,” *Journal of Materials Processing Technology*, vol. 238, pp. 437–445, Dec. 2016, doi: 10.1016/j.jmatprotec.2016.08.003.
[79] Y. Otani and S. Sasaki, “Effects of the addition of silicon to 7075 aluminum alloy on microstructure, mechanical properties, and selective laser melting processability,” *Materials Science and Engineering: A*, vol. 777, p. 139079, Mar. 2020, doi: 10.1016/j.msea.2020.139079.
[80] Y. Otani and S. Sasaki, “Effects of the addition of silicon to 7075 aluminum alloy on microstructure, mechanical properties, and selective laser melting processability,” *Materials Science and Engineering: A*, vol. 777, p. 139079, Mar. 2020, doi: 10.1016/j.msea.2020.139079.
[81] X. Nie, H. Zhang, H. Zhu, Z. Hu, L. Ke, and X. Zeng, “Effect of Zr content on formability, microstructure and mechanical properties of selective laser melted Zr modified Al-4.24Cu-1.97Mg-0.56Mn alloys,” *Journal of Alloys and Compounds*, vol. 764, pp. 977–986, Oct. 2018, doi: 10.1016/j.jallcom.2018.06.032.
[82] M. L. Montero-Sistiaga *et al.*, “Changing the alloy composition of Al7075 for better processability by selective laser melting,” *Journal of Materials Processing Technology*, vol. 238, pp. 437–445, Dec. 2016, doi: 10.1016/j.jmatprotec.2016.08.003.
[83] D. R. Manca, A. Yu. Churyumov, A. V. Pozdniakov, D. K. Ryabov, V. A. Korolev, and D. K. Daubarayte, “Novel heat-resistant Al-Si-Ni-Fe alloy manufactured by selective laser melting,” *Materials Letters*, vol. 236, pp. 676–679, Feb. 2019, doi: 10.1016/j.matlet.2018.11.033.

[84] L. Li *et al.*, “Microstructures and mechanical properties of Si and Zr modified Al–Zn–Mg–Cu alloy-A comparison between selective laser melting and spark plasma sintering,” *Journal of Alloys and Compounds*, vol. 821, p. 153520, Apr. 2020, doi: 10.1016/j.jallcom.2019.153520.
[85] J. Deng, C. Chen, X. Liu, Y. Li, K. Zhou, and S. Guo, “A high-strength heat-resistant Al−5.7Ni eutectic alloy with spherical Al3Ni nano-particles by selective laser melting,” *Scripta Materialia*, vol. 203, p. 114034, Oct. 2021, doi: 10.1016/j.scriptamat.2021.114034.
[86] J. Fiocchi, A. Tuissi, and C. A. Biffi, “Heat treatment of aluminium alloys produced by laser powder bed fusion: A review,” *Materials & Design*, vol. 204, p. 109651, Jun. 2021, doi: 10.1016/j.matdes.2021.109651.
[87] N. T. Aboulkhair, M. Simonelli, L. Parry, I. Ashcroft, C. Tuck, and R. Hague, “3D printing of Aluminium alloys: Additive Manufacturing of Aluminium alloys using selective laser melting,” *Progress in Materials Science*, vol. 106, p. 100578, Dec. 2019, doi: 10.1016/j.pmatsci.2019.100578.
[88] T. Sercombe, N. Jones, R. Day, and A. Kop, “Heat treatment of Ti-6Al-7Nb components produced by selective laser melting,” *Rapid Prototyping Journal*, vol. 14, no. 5, pp. 300–304, Sep. 2008, doi: 10.1108/13552540810907974.
[89] N. T. Aboulkhair, I. Maskery, C. Tuck, I. Ashcroft, and N. M. Everitt, “The microstructure and mechanical properties of selectively laser melted AlSi10Mg: The effect of a conventional T6-like heat treatment,” *Materials Science and Engineering: A*, vol. 667, pp. 139–146, Jun. 2016, doi: 10.1016/j.msea.2016.04.092.
[90] N. T. Aboulkhair, C. Tuck, I. Ashcroft, I. Maskery, and N. M. Everitt, “On the Precipitation Hardening of Selective Laser Melted AlSi10Mg,” *Metallurgical and Materials Transactions A*, vol. 46, no. 8, pp. 3337–3341, Aug. 2015, doi: 10.1007/s11661-015-2980-7.
[91] M. Bayat *et al.*, “Keyhole-induced porosities in Laser-based Powder Bed Fusion (L-PBF) of Ti6Al4V: High-fidelity modelling and experimental validation,” *Additive Manufacturing*, vol. 30, p. 100835, Dec. 2019, doi: 10.1016/j.addma.2019.100835.
[92] B. Basu, G. B. Raju, and A. K. Suri, “Processing and properties of monolithic TiB_2 based materials,” *International Materials Reviews*, vol. 51, no. 6, pp. 352–374, Dec. 2006, doi: 10.1179/174328006X102529.
[93] *Functionally Graded Materials 1996*. Elsevier, 1997. doi: 10.1016/B978-0-444-82548-3.X5000-8.
[94] Z. Feng, H. Tan, Y. Fang, X. Lin, and W. Huang, “Selective laser melting of TiB2/AlSi10Mg composite: Processability, microstructure and fracture behavior,” *Journal of Materials Processing Technology*, vol. 299, p. 117386, Jan. 2022, doi: 10.1016/j.jmatprotec.2021.117386.
[95] D. Gu, F. Chang, and D. Dai, “Selective Laser Melting Additive Manufacturing of Novel Aluminum Based Composites With Multiple Reinforcing Phases,” *Journal of Manufacturing Science and Engineering*, vol. 137, no. 2, Apr. 2015, doi: 10.1115/1.4028925.
[96] L. P. Lam, D. Q. Zhang, Z. H. Liu, and C. K. Chua, “Phase analysis and microstructure characterisation of AlSi10Mg parts produced by Selective Laser Melting,” *Virtual and Physical Prototyping*, vol. 10, no. 4, pp. 207–215, Oct. 2015, doi: 10.1080/17452759.2015.1110868.